

This is an Open Access document downloaded from ORCA, Cardiff University's institutional repository: <https://orca.cardiff.ac.uk/id/eprint/124701/>

This is the author's version of a work that was submitted to / accepted for publication.

Citation for final published version:

Dodd, Matthew S., Papineau, Dominic, She, Zhenbing, Fogel, Marilyn L., Nederbragt, Sandra and Pirajno, Franco 2018. Organic remains in late Palaeoproterozoic granular iron formations and implications for the origin of granules. *Precambrian Research* 310 , pp. 133-152. 10.1016/j.precamres.2018.02.016

Publishers page: <https://doi.org/10.1016/j.precamres.2018.02.016>

Please note:

Changes made as a result of publishing processes such as copy-editing, formatting and page numbers may not be reflected in this version. For the definitive version of this publication, please refer to the published source. You are advised to consult the publisher's version if you wish to cite this paper.

This version is being made available in accordance with publisher policies. See <http://orca.cf.ac.uk/policies.html> for usage policies. Copyright and moral rights for publications made available in ORCA are retained by the copyright holders.



# Organic remains in late Palaeoproterozoic granular iron formations and implications for the origin of granules

Matthew S Dodd<sup>a,b</sup>, Dominic Papineau<sup>a,b</sup>, Zhenbing She<sup>c</sup>, Marilyn L. Fogel<sup>d</sup>, Sandra Nederbragt<sup>e</sup>, Franco Pirajno<sup>f</sup>,

<sup>a</sup>London Centre for Nanotechnology, 17-19 Gordon Street, University College London, London, WC1H 0AH, UK.

<sup>b</sup>Department of Earth Sciences, University College London, London, WC1E 6BT, UK.

<sup>c</sup>School of Earth Sciences & State Key Laboratory of Biogeology and Environmental Biology, China University of Geosciences, Wuhan, China.

<sup>d</sup>Department of Earth Sciences, University of California, Riverside 900 University Ave. Riverside, CA 92521, USA

<sup>e</sup>School of Earth and Ocean Sciences, Cardiff University, Cardiff, CF10 3AT, UK.

<sup>f</sup>Centre for Exploration Targeting, The University of Western Australia, 35 Stirling Highway, Crawley, WA 6009 Australia

**Keywords:** iron formation, Proterozoic, microfossil, carbon isotopes, granules

**Toward the end of the Palaeoproterozoic era, over 10<sup>9</sup> billion tonnes of banded (BIF) and granular (GIF) iron formations were deposited on continental platforms. Granules in iron formations are typically sub-spherical structures 0.2 to 10 mm in size, whereas concretions are larger than 10mm. Both types of spheroids are preserved throughout the sedimentological record. Their formation has typically been interpreted to originate from reworked Fe-rich sediments in high-energy, wave-agitated, shallow-marine environments. New evidence from six different late Palaeoproterozoic granular iron formations (GIF), however, suggests that some granules are the result of diagenetic reactions, in addition to other features driven by microbial processes and mechanical movements. Characteristic coarse grain interiors and septarian-type cracks inside granules, akin to those features in decimetre- to meter-size concretions, are interpreted as dessication features from hydrated diagenetic environments where sulphate and/ or ferric iron were reduced while organic matter (OM) was oxidised inside granules. Those granules derived from sulphate reduction preserve diagenetic pyrite rims, whereas those formed via ferric iron reduction preserve diagenetic magnetite along their rims. Other diagenetic minerals including apatite mixed with OM, and various carbonate phases are commonly preserved within**

granules. Combined with systematically  $^{13}\text{C}$ -depleted carbonate, these diagenetic mineral assemblages point to the oxidative decay of OM as a major process involved in the formation of granules. Spheroidal equidistant haematite laminations surround some granules and contain apatite associated with carbonate, OM, and ferric-ferrous silicates, and oxides that further suggest these structures were not shaped by wave-action along sediment-water interfaces, but rather by chemical wave fronts and biomineralisation. Our results demonstrate that the formation mechanisms of GIF also involve microbial activity and chemically-oscillating reactions. As such, granules have excellent potential to be considered as promising biosignatures for studying Precambrian biogeochemistry, as well as astrobiology.

## **1.0 Introduction**

Granules are common textures in a variety of chemical sedimentary rocks (Lougheed, 1983; She et al., 2013) and are found from the beginning of the sedimentary rock record through to present day sediments (Pye et al., 1990). Their association with some of the earliest evidence for microbial life on Earth (Schopf and Kudryavtsev, 2012) make them an important sedimentological feature in astrobiological studies. A number of terms have been used to describe granular textures in sedimentary rocks, such as ooid, pisoid, peloid, oncoid, nodule or concretion. The array of terms reflects their variably interpreted origins and the diversity of structures for different spheroidal sedimentary features (Neuendorf et al., 2005). The origin of granules in granular iron formations (GIF) is debated as to whether they reflect sediment reworking (Akin et al., 2013; Simonson, 2003), mineral precipitation (Stefurak et al., 2015) or biological origins (Dahanayake and Krumbein,

1986; Salama et al., 2013). Herein we adopt the term granule for all spheroidal sedimentary structures 0.2-10mm in size. Larger granules (i.e. >10mm in size) are referred to as concretions.

Granular iron formations increased in abundance from ca. 2,000 to 1,500 Myr ago in the aftermath of the Great Oxidation Event (Trendall, 2002), during a period of intense global volcanism (Rasmussen et al., 2012). However GIF have also been recognised in much older deposits, for example in the ca. 2,460 Myr Kuruman-Griquatown IF, South Africa (Beukes and Klein, 1990; Pickard, 2003) and the ca. 2,940 Myr Witwatersrand-Mozaan basin, South Africa (Beukes and Cairncross, 1991; Smith et al., 2017). The occurrence of GIFs, in association with shallow-marine sediments with current-generated structures, has led to the conclusion by some that granules in these rocks represent sediments disrupted by currents and wave action (Akin et al., 2013; Lascelles, 2007; Pufahl and Fralick, 2004; Simonson, 2003), while granules with irregular layering in GIFs have been attributed to stromatolitic growth of microbial colonies (Smith et al., 2017; Walter et al., 1976). Others have proposed that some Precambrian granules may represent a unique style of silica precipitation, whereby stages of silica aggregation of nanospheres, prompted by changes in water chemistry, produced episodic granule formation (Stefurak et al., 2015). Alternatively, the curved, equidistant laminations around granules may be explained by diagenetic growth during oxidation of OM. These processes may be biologically-mediated or abiotic reactions proceeding as chemically-oscillating reactions such as the Belousov-Zhabotinsky (B-Z) reaction (Zaikin and Zhabotinsky, 1970), as was suggested for the formation of rosettes and granules in the Lake Superior area (Papineau et al., 2017). The B-Z oscillating type reactions proceed with solutions containing, for example, malonic acid, sulphate and bromate-bromide. These reactions produce a switch in the oxidation state of ferroin, which is used in

the reaction to see changes in redox state between periodic oxidised fronts. Their patterns are fractal as they repeat in shape and size proportion at different length scales, and can be described as curved equidistant laminations that propagate outward as chemical waves. In light of this and the potential role of microbial activity in GIFs we describe the characteristics of granules, the microfossils found within, and their mineralogy in six different IFs from around the world during the late Palaeoproterozoic.

## **2.0 Geological setting of the six studied late Palaeoproterozoic GIFs**

All granular IFs described in this study formed in separate, tectonically active basins, between 2.0 Ga and 1.6 Ga along shallow continental shelves and are stratigraphically associated with major stromatolitic horizons.

### **2.1 Chuanlinggou iron formation**

The Chuanlinggou IF (also known as Xuanlong-type iron deposit) is part of the Changcheng Group and located in north-western Hebei province, China (Luo et al., 2014). The Chuanlinggou Fm. is 40-90m thick and comprises a lower ore section of granular and stromatolitic ironstones and upper shale member (Fig. 1A-D; 2A; 3A-C). This ore section is composed of siltstones, sandstones and ferruginous sandstones intercalated with beds of iron ore. Each ore bed is typically composed of a lower GIF layer with an upper part dominated by stromatolitic iron formation and at the top of each bed occurs a thin layer of siderite. Ripple marks and mud cracks now filled with chert and carbonate occur in the light green mudstone between iron ore beds suggestive of a shallow-marine to intertidal depositional setting. The formation was deposited in the Yanshan continental rift basin between  $1638 \pm 14$  Ma and  $1673 \pm 10$  Ma based on U-Pb dating of diabase in the Chuanlinggou Fm (Gao et al., 2009) and intrusive granite dykes (Li et al., 2011). This

continental rift basin has been linked to the initial breakup of the supercontinent Nuna from 1.6-1.2 Ga (Kusky and Li, 2003). The samples were collected from Pangjiapu quarry, Zhangjiakou city, Hebei Province (40°37'42.16"N, 115°27'49.29"E).

## **2.2 Biwabik iron formation**

The Biwabik IF forms part of the Palaeoproterozoic Animikie Group in the Lake Superior region of the USA and Canada. It is one of many separate but coeval IFs deposited in the group. The age of the IF is constrained by U-Pb dating from associated volcanic beds bounding the formations, yielding minimum and maximum ages of 1874±9 Ma (Schneider et al., 2002) and 1878±1.3 Ma (Fralick et al., 2002). The Biwabik Fm consists of two repeating horizons of iron formations (Fig. 2B) occurring as stromatolite beds with intercolumnar granules (lower and upper cherty units) and granular to concretionary ferruginous argillaceous chert beds (Pufhal et al., 2004). These iron formations are believed to have been deposited in shallow water continental shelf environments in volcanically active basins during the onset of the Penokean Orogen (Schulz and Cannon, 2007). The IFs stratigraphically occur with quartzite and carbonaceous siltstones (Fig. 2B), interpreted to represent shore and continental slope deposits respectively (Ojakangas, 1983; Pufahl and Fralick, 2004). The Biwabik IF preserves columnar stromatolite with diameters between 0.5 to 3 cm and intercolumns and interbeds filled with iron-oxide granules and concretions (Fig. 1E-F; 3E-F) (Gruner, 1924; Loughheed, 1983; Shapiro and Konhauser, 2015). Samples were collected from mine tailings, in the Mary Ellen and Thunderbird mines, from the 'lower cherty' member (Ojakangas, 1983) of the Biwabik Fm.

## **2.3 Nastapoka and Kipalu iron formations**

The Nastapoka and Kipalu IFs outcrop along the eastern shore of Hudson Bay, Canada, and have been stratigraphically correlated (Chandler and Parrish, 1989). The Nastapoka Group is an approximately 800m thick sequence including stromatolitic dolomite, sandstone, mafic flows and IF (Fig. 1H; 2C; 3H-I). The age of the IF in the Nastapoka group is constrained between 1870 Ma, from U-Pb in baddeleyite from the Flaherty basalt correlative with the basalt overlying the Nastapoka IF (Hamilton et al., 2009), and  $2025 \pm 25$  Ma, from U-Pb in uraniferous apatite cement from an arkosic sandstone in the Pachi Formation (Chandler and Parrish, 1989). The Nastapoka Group was deposited in a volcanically active rift basin, above volcanic rocks in the Richmond Gulf graben (Chandler, 1981, 1984). The studied samples came from the Clark Island (*NgCi11002*: N56°26'28.0", W76°38'05.6" and *NgCi11003*: N56°26'47.0", W76°37'59.6"), which is part of the chain of Nastapoka Island.

The Kipalu IF in the Belchers group outcrops in the Belcher Islands, along the eastern margins of Hudson Bay and are overlain by thick basalt flows of the Flaherty Formation and turbidites from the Omarrolok Formation (Fig. 1G; 2D; 3G) (Chandler, 1984) deposited during the Trans-Hudsonian Orogen and the assembly of the Nuna supercontinent (Ernst and Bleeker, 2010). The GIF occurs as concretionary lenses in Fe-silicate banded iron formation and overlies sandstones of the Mukpollo and Rowatt formations. It is also underlying columnar and pillow basalt of the Flaherty Fm, which is suggested to have been deposited as a result of rifting (Baragar and Scoates, 1981; Chandler, 1981). Additionally, red beds of siliciclastic sediments below the IFs have been used to suggest the atmosphere contained significant free oxygen before deposition of the IFs (Chandler, 1981). The studied sample *BgKi11002* came from N56°13'43.5", W78°40'09.7" (Fig. 1G).

## **2.4 Akaitcho River iron formation**

The IF occurs near the transition between the Akaitcho River and Seton formations, respectively in the Sosan and Kahochella groups, in the Great Slave Lake Supergroup, Northwest Territories, Canada. Rb-Sr isotopic measurements give an age of  $1872 \pm 10$  Myr for the eruption of spilitic basalts in the Seton Formation (Baadsgaard et al., 1973), giving a minimum age for the GIF. The GIFs forms 30cm thick interbeds and lenses between cross-bedded sandstones and are associated with shallow marine shales (Fig. 1I; 2E; 3D), along with andesitic, pyroclastic volcanics sometimes associated with Cu-sulphide mineralization (Roscoe et al., 1987). The Great Slave Lake Supergroup formed in a graben between 2000 to 1800 Myr ago (Bowring et al., 1984) and the association of conglomerates, cross-bedded and rippled sandstone with gypsum casts demonstrates these sedimentary units were deposited in shallow water settings (Hoffman, 1968). The granular IFs occur stratigraphically above major stromatolite-bearing horizons of the Duhamel Fm and below the prolific stromatolites of the Pethei Group (Hoffman, 1968). The studied sample GS1025 was collected from an outcrop located at N62°02'16.5", W111°58.3'31.8".

## **2.5 Frere iron formation**

The Frere Fm (Fig. 1J-L; 2F; 3J-N) was deposited in the Earraheedy basin of Western Australia (Pirajno et al., 2009), along the Capricorn Orogen between the Yilgarn and Pilbara cratons. Deposition took place around  $1,891 \pm 8$  Myr ago (Rasmussen et al., 2012), during tectonic rifting and marine transgression. The Frere Fm overlies the stromatolitic dolomite of the Yelma Fm (Pirajno et al., 2009) and transitions into the stromatolitic carbonate, shale and siltstone beds of the Windidda member which also has minor granular IF beds (Pirajno



et al., 2009). The IF is interpreted to have been deposited almost entirely within the peritidal zone with lenses of trough, cross-stratified GIF preserved in laminated magnetite-chlorite siltstone (Akin et al., 2013). The recognition of Gunflint-type microbiota in the Frere Fm (Tobin, 1990; Walter et al., 1976) suggests deposition in coastal palaeoenvironments similar to the Gunflint and Biwabik IFs in North America.

### **3.0 Analytical methods**

Over 100 thin sections were cut from fresh rock samples or cores, and a small selection with variable haematite content was analysed in detail (Fig. 3). Thin sections were cut to 30  $\mu\text{m}$  thickness and polished to 0.25  $\mu\text{m}$  with  $\text{Al}_2\text{O}_3$  powder in DI water. Cover slips were not used in sample preparation and oil immersion was not used during analytical measurements.

#### **3.1 *Optical and micro-Raman microscopy***

An Olympus BX51 microscope with 5X, 10X, 20X, 50X and 100X objectives was used to conduct transmitted and reflected light optical microscopy on polished thin sections and all micro-Raman analyses were performed before Au-coating for analysis by Scanning Electron Microscopy (SEM). Micro-Raman imaging was conducted at the London Centre for Nanotechnology in University College London with a WITec  $\alpha 300$  Confocal Raman Imaging system. A 532nm laser was used with a power less than 6mW and was focused at 200X for large area scans ( $>600 \times 600 \mu\text{m}$ ) and 1000X for smaller area scans, achieving spatial resolutions between 2000 and 360 nm. A 50  $\mu\text{m}$  thick optic fibre cable was used to collect Raman spectra at confocal depths of at least one  $\mu\text{m}$  below the surface of the thin sections. Each pixel collected a Raman spectrum with a typical dwell time of 0.5 seconds. All Raman spectra were corrected for cosmic rays using the cosmic ray reduction function in the WITec

Project Four Plus software. All Raman spectra herein were selected from pixels with nearly identical spectra. The averaged spectra were corrected with a background subtraction polynomial fit, typically of order 4 to 7. Raman spectrum parameters, such as peak positions, Full Width at Half Maximum (FWHM), and areas under the curve were extracted from the best-resolved Raman peaks modelled with a Lorentzian function on background-corrected spectra. Raman hyperspectral images of mineral associations were generated by mapping peak intensities for the strongest or unique mineral-specific peaks (pyrite – 376  $\text{cm}^{-1}$ , goethite – 394  $\text{cm}^{-1}$ , chamosite – 550  $\text{cm}^{-1}$ , muscovite – 701  $\text{cm}^{-1}$ , illite – 707  $\text{cm}^{-1}$ , quartz – 465  $\text{cm}^{-1}$ , greenalite – 648  $\text{cm}^{-1}$ , magnetite/ stilpnomelane – 667  $\text{cm}^{-1}$ , minnesotaite – 678  $\text{cm}^{-1}$ , ferrihydrite – 681  $\text{cm}^{-1}$ , apatite – 965  $\text{cm}^{-1}$ , calcite – 1088  $\text{cm}^{-1}$ , siderite – 1092  $\text{cm}^{-1}$ , ankerite – 1097  $\text{cm}^{-1}$ , dolomite – 1100  $\text{cm}^{-1}$ , haematite – 1320  $\text{cm}^{-1}$ , OM – 1600  $\text{cm}^{-1}$ ) using the WITec Project Four Plus data processing software.

All Raman peak positions were read directly from average spectra calculated from representative regions with high signal-to-noise after background removal. To estimate maximum crystallisation temperatures of organic matter (OM) from Raman spectra, we used the geothermometer of Lahfid et al. (2010) and Rahl et al. (2005), which is justified by the prehnite-pumpellyite to lower greenschist metamorphic grade of all the studied granular IF. The following peaks were used: D1 (around 1330-1350  $\text{cm}^{-1}$ ), G + D2 (around 1580-1610 and 1620  $\text{cm}^{-1}$ , respectively). The D3 peaks at around 1510  $\text{cm}^{-1}$  and the D4 peak around 1245  $\text{cm}^{-1}$  used in the geothermometry models developed by (Kouketsu et al., 2014; Lahfid et al., 2010; Rahl et al., 2005) were not-resolved, but they were extracted still from Lorentz-fitted functions. Peak areas reported come from the integration of these Lorentz functions and were fitted to the measured spectra as linear combinations over the 1000-2000  $\text{cm}^{-1}$  spectral range.

### **3.2 Isotope analysis of organic matter and carbonates**

Analyses of bulk rock powders for OM were conducted in the Bloomsbury Environmental Isotope Facility at UCL with a Thermo-Finnigan Flash 1112 EA connected to a Thermo Delta V Isotope Ratio Mass Spectrometer via a ConFlo IV gas distribution system. OM was obtained by dissolving about 30 to 80 mg of bulk powder (crushed with a steel mortar and pestle cleaned with muffled quartz chips between samples) in Ag boats, pre-muffled at 600°C for 2 hours, with 10% ultrapure HCl followed by air drying in a laminar air flow hood. The dried residue was then loaded into a second muffled silver capsule, and then placed into an autosampler and dropped into the furnace of the Thermo-Finnigan Flash 1112 EA. An ultrapure He carrier gas was used for the procedure in continuous flow mode. Two reactors were used to generate CO<sub>2</sub> with the first oxidising reactor packed with Cr<sub>2</sub>O<sub>3</sub> and silvered cobalt oxide. A second reactor filled with elemental Cu was a reduction furnace heated at (680°C). Lastly, the evolved gas passed through a water trap of magnesium perchlorate, before injection to the mass spectrometer via a ConFlo IV interface, for further details see Papineau et al., 2016.

A suite of standard materials were analysed within each run that span a range of  $\delta^{13}\text{C}$  values from -26‰ to -6‰. Each standard is analysed multiple times through the run to ensure reproducibility and precision. The results were calibrated to the VPDB scale with a reproducibility better than 0.2‰ (1 $\sigma$ ; n=19). Empty muffled silver capsules were run with and without HCl added to test for contamination prior to analysis. No C was detected in these procedural blank silver capsules.

Analyses of bulk rock powders for carbonate were conducted in the Cardiff School of Earth Sciences with a Thermo Finnigan Delta V Advantage mass spectrometer connected to a Gas Bench II. Samples in vials were acidified with >99% H<sub>3</sub>PO<sub>4</sub> by manually injecting the acid using a syringe. All samples and standards were left to react for 4 days at 60°C before analysis. The reproducibility for  $\delta^{13}\text{C}_{\text{carb}}$  and  $\delta^{18}\text{O}_{\text{SMOW}}$  was better than  $\pm 0.1\text{‰}$  ( $1\sigma$ ), based on multiple measurements of an in-house standard of Carrara marble (calcite). Measured  $^{18}\text{O}/^{16}\text{O}$  ratios were corrected for mineralogy, inferred from SEM analyses (see below), using acid fractionation – temperature equations from Fernandez et al., 2016 (siderite); Rosenbaum and Sheppard, 1986 (ankerite) and Kim et al., 2015 (calcite).

### **3.3 Scanning Electron Microscopy (SEM) and Energy Dispersive Spectroscopic (EDS) analyses**

SEM analyses were performed using a JEOL JSM-6480L SEM in the Department of Earth Sciences at University College London. Operating conditions for SEM imaging and EDS analysis involved a 15kV accelerating voltage for an electron beam current of 1nA, with a working distance of around 10mm. Polished thin sections were cleaned with isopropyl alcohol and dried with dry N<sub>2</sub>, before deposition of a few nanometres of Au (1 or 2 minutes coating under a current of about 1.8 mA in Ar) subsequent to SEM analyses. The EDS instrument used was an Oxford Instrument 80 mm<sup>2</sup> silicon drift detector. Data points were calculated by software using ZAF correction and normalized to 100.0 %, which yield an error of around 5%.

## **4.0 Results**

#### 4.1 Petrology and geochemistry of granules in the Chuanlinggou iron formation

The Chuanlinggou IF specimens analysed were ferruginous sandstones associated with stromatolites and oolites. Detrital quartz grains range in size between 200-500  $\mu\text{m}$  and have a sub-angular habit and are poorly sorted (Fig. 4A). The sandstone is cemented with siderite in the less iron-oxide rich samples (Fig. 4A-G) and goethite and haematite in the most iron-oxide rich samples (Fig. 4H-I). Rounded zircon grains of detrital origin co-occur with similar-size rounded quartz grains and have also been found in the less iron-rich samples (Fig. 4G). Carbonaceous coatings on quartz grains are common and typically associated with haematite, illite, siderite and minor apatite (Fig 4B). Haematite and goethite granules exhibit concentric laminations of iron-oxide, which occur around quartz grains, whereas others have no central core or some granules have multiple quartz grains around which concentric laminations occur (Fig 4H-I). The granule shapes vary from angular to sub-spheroidal (Fig. 4H-I). The layering varies from condensed grey haematite to sparse goethite infilled layers. Multiple granules are commonly bound together by iron-oxide layers that envelope them (Fig. 4I).

Rare occurrences of siderite-haematite granules in between quartz clasts exhibit micron-scale layering of acicular haematite crystals, which form aggregates of variably-oriented nanoscopic haematite and illite (Fig. 4D-F). In sample *CHG1502-3* (Fig. 3B) the intergranular siderite is Mg-rich varying from 4.8 to 12.7 wt% Mg (Table 1) and has  $\delta^{13}\text{C}_{\text{carb}}$  ranging from -7.6 to -8.5‰ and  $\delta^{18}\text{O}_{\text{SMOW}}$  of +21.1 to +15.2‰ (Table 2). OM is present either as micron-wide veinlets in siderite, or as concentric outer layers in granules (Fig. 4E). In these Fe-rich sandstones, the TOC is low and around 0.04 wt%, whereas the more Fe-rich

granular iron formation also have low TOC around 0.03 wt% and  $\delta^{13}\text{C}_{\text{org}}$  values between -21.7 to -28.0‰ (Table 2).

Siderite beds occur at the top of the granular and stromatolitic iron formation bed packages in the Chuanlinggou and host granules of siderite (Fig. 5A). Siderite crystals inside these granules are coarse, ranging in size from 100 to 600  $\mu\text{m}$ , whereas the siderite matrix is micritic and distinctly finer grained ( $< 4 \mu\text{m}$ ) (Fig. 5A-B). Coarse siderite granules have rims of spheroidal shaped pyrite with concentric laminations (Fig. 5B), which may partially or completely surround the granule. The rims of other coarse siderite granules are formed of fine tangentially-radiating siderite, which sometimes concentrically encloses a clay layer (about 40  $\mu\text{m}$  thick) and/or an OM layer (80  $\mu\text{m}$  thick) (Fig. 5C). Sub-rounded detrital quartz clasts are found inside some granules (Fig. 5A, 5C-E) and in the matrix, sometimes with coatings of OM. When present, these OM coatings penetrate into the quartz grains and form concentric rings of OM inside the quartz grains (Fig. 5E). OM occurs in both the granules and matrix (Fig. 5G-H). The chemical composition of the siderite varies from Mg-bearing siderite (ca. 5wt % Mg) inside the granules, to Mn-bearing siderite (ca. 3wt % Mn) in the matrix (Fig. 5I) (Table 1). Within the granules the Raman spectrum of OM shows a typical kerogen spectrum, with a broad, intense D1-peak at  $1348 \text{ cm}^{-1}$ , a similarly intense G-peak at around  $1606 \text{ cm}^{-1}$  and minor 2D peaks around  $2700 \text{ cm}^{-1}$ . Using the Rahl et al. (2005) and Lafhid et al. (2010) Raman thermometers, Raman spectra were used to calculate a peak metamorphic temperature between 198-274°C (Table 3), consistent with metamorphism at the prehnite-pumpeleyite to sub-greenschist facies. OM in the matrix has a Raman spectrum with unresolved D and G-peaks, which merge into a broad peak centred at  $1430 \text{ cm}^{-1}$  (Fig. 5H). The TOC of the siderite GIF is considerably higher than the other Chuanlinggou samples,

reaching between 0.16-0.21 wt% and its  $\delta^{13}\text{C}_{\text{org}}$  values between -27.9‰ and -29.9‰. Bulk siderite has  $\delta^{13}\text{C}_{\text{carb}}$  and  $\delta^{18}\text{O}_{\text{SMOW}}$  values of -9.3‰ and +22.3‰, respectively (Table 2).

## **4.2 Petrology and geochemistry of granules and concretions in the Biwabik iron formation**

Granules in the Biwabik jasper occur between stromatolite columns, similar to carbonate ooids between stromatolite columns in carbonates from the Phanerozoic (Paul et al., 2011). Most granules in the IFs exhibit interiors of coarse quartz ranging in size from 50  $\mu\text{m}$  to 500  $\mu\text{m}$ , in contrast to their surrounding fine (<40  $\mu\text{m}$ ) chert matrix (Fig. 6A-B; 7B), which indicates longer growth times for intragranular quartz compared to intergranular chert. Multiple granules are sometimes bound by concentric layers that envelope the granules (Fig. 6A), but this is less common than in the Chuanlinggou GIF. Equally, large irregular and thick (3mm) haematite layers encapsulate numerous larger granules, even forming concretions (> 10mm) (Fig. 3F, 7A). The inner rims of these concretions are formed of magnetite or haematite, which are also sporadically found throughout the interior (Fig. 7A, B). Both the surrounding matrix and granules are speckled with nanoscopic grains of haematite, while magnetite almost always occurs along the rims of granules or concretions and rarely in the centres (Fig. 6C-E, 7B)(Papineau et al., 2017). Some granules exhibit concentric layering formed of nanoscopic haematite and phyllosilicates with inclusions of OM (Fig. 6F-H). Additionally, OM occurs as inclusions in apatite inside some granules (Fig. 6E; 7E). Infrequently, granules display finely-laminated and broadening columns akin to stromatolites along their rims (Fig. 7C), within which OM-bearing apatite and carbonate is concentrated compared to the matrix, and similar to granule interiors (Fig. 7D-F). Shrinkage cracks are common features in granules from the Biwabik jaspers, cutting through all layers

in the granule rims (Fig. 7A). OM in the Biwabik GIF samples displays equally intense D1 and G peaks with D1-peaks around  $1340\text{ cm}^{-1}$  and G-peaks from  $1596$  to  $1616\text{ cm}^{-1}$ , with minor 2D peaks (Fig. 6I, 7G), yielding peak metamorphic temperatures of  $251\text{--}291^\circ\text{C}$  (Table 3), calculated using the Lahfid thermometer. The TOC of the Biwabik IFs is low and ranges from  $0.02$  to  $0.04\text{wt\%}$ , while the  $\delta^{13}\text{C}_{\text{org}}$  values are fairly consistent with an average of  $-28.0\text{‰}$ . Carbonate isotopic compositions are  $-12.3\text{‰}$  and  $+18.1\text{‰}$  for  $\delta^{13}\text{C}_{\text{carb}}$  and  $\delta^{18}\text{O}_{\text{SMOW}}$  respectively (Table 2).

#### **4.3 Petrology and geochemistry of granules in the Nastapoka iron formation**

Similar to the Biwabik IF granules, the Nastapoka granules also have coarse quartz interiors relative to the fine chert matrix (Fig. 8A-C). Typically the granules with the coarsest interiors have the thickest magnetite rims and contain mainly only quartz, siderite/ ankerite, and minnesotaite as intragranular minerals. The granules also commonly have concentric layers of nanoscopic haematite which envelope the coarse, euhedral magnetite rims and bind multiple granules together (Fig. 8C), similarly to Biwabik granules. Both these concentric haematite and magnetite granular rims are commonly cut by inward-fining V-shaped indentations, similar to septarian shrinkage cracks in concretions. These are outlined by nanoscopic haematite and are filled with finer chert than the coarse quartz interior (Fig. 8B). Siderite rhombohedra have ubiquitous poikilitic inclusions of haematite and magnetite in both the matrix and inside granules which they overgrow (Fig. 8C). Carbonate occurs as siderite and makes up less than  $0.15\%$  of the total sample (Table 2). Minnesotaite  $[(\text{Fe}, \text{Mg})_3\text{Si}_4\text{O}_{10}(\text{OH})_2]$  occurs in the matrix and as needles cutting across the rims of granules (Fig. 8C).



In clay-rich samples from the Nastapoka IF, granules are composed of thick red haematite rims with interiors of quartz, fine-grained minnesotaite (Table 1) and carbonate with OM disseminations throughout the minnesotaite and carbonate (Fig. 8D-J). Other Nastapoka granules are formed of dense grey haematite (Fig. 8E). Organic matter in Nastapoka GIF has broad and intense D1-band Raman peaks around  $1331\text{ cm}^{-1}$  and sharp, intense G-peaks around  $1607\text{ cm}^{-1}$ , which give crystallisation temperatures of  $248\text{--}300^{\circ}\text{C}$  (Table 3), consistent with sub-greenschist facies metamorphism. The TOC of these samples varies considerably between the clay-rich samples with up to 0.27wt% TOC and less clay-rich samples with more typical low TOC around 0.02wt% (Table 2). Likewise the  $\delta^{13}\text{C}$  values of the OM are also distinct with values as negative as  $-36.1\text{‰}$  in the clay-rich sample (Ngci1002) and  $-26.4\text{‰}$  in the oxide-rich sample (Ngci1003).

#### **4.4 Petrology and geochemistry of granules in the Kipalu granular iron formation**

Granules in the Kipalu GIF are markedly different from those in the Biwabik and Nastapoka GIF. They are predominately composed of chert, with haematite that occurs as variably-shaped spheroidal to sub-rounded granules of chert and haematite (Fig. 9A). Chert is sometimes coarsest in intergranular space where it forms isopachous textures (Fig. 9A), distinct from the other GIF studied in this work and also from the detrital intergranular matrix of the iron-oxide Chuanlinggou GIF. Within the chert matrix between granules, there are sub-rounded detrital quartz grains up to  $200\text{ }\mu\text{m}$  in size (Fig. 9G). Rarely, some granules exhibit inward fining V-shaped structures akin to shrinkage cracks (Fig. 9H), and coarse quartz interiors which are similar to those of the Nastapoka GIF. However most of the granules predominately contain microcrystalline chert with either densely packed grey and red haematite or finely disseminated haematite.

Filaments of haematite form discrete clusters within granules (Fig. 9B) and some filaments emanate from granules and/ or stretch between them (Fig. 9C-D), cutting across the isopachous intergranular quartz. The filaments have diameters of 6-8  $\mu\text{m}$ , lengths up to 300  $\mu\text{m}$ , and they commonly are straight with rare bends or curvature. Granules associated with filaments sometimes contain small amounts of OM, which occurs as micron-sized particles that have broad D1-peaks centred at 1340  $\text{cm}^{-1}$  and sharp G-peaks around 1588  $\text{cm}^{-1}$  (Fig. 9F), giving peak metamorphic temperature estimates between 212-295°C (Table 3). The TOC contents are low, around 0.02-0.03wt%, and have a small range of  $\delta^{13}\text{C}$  values from -28.0 to -28.8‰ (Table 2). Lastly, sub-rhombohedral carbonate rosettes up to 200  $\mu\text{m}$  in diameter are found between granules within the chert matrix (Fig. 9J). The carbonate has ankerite composition, estimated from Raman spectra, along with  $\delta^{13}\text{C}_{\text{Carb}}$  and  $\delta^{18}\text{O}_{\text{SMOW}}$  values of -9.0‰ and +21.4‰ respectively (Table 2).

#### **4.5 Petrology and geochemistry of the Akaitcho River granular iron formation**

The Akaitcho River GIF has granules texturally most similar to those in the Kipalu GIF, but also have their unique characters. The Akaitcho River granules are composed predominately of chert and densely compacted nanoscopic grains of red or grey haematite, which form irregular and pinching-and-swelling shaped granules (Fig. 10A). Between granules, chamosite and muscovite occur along with microscopic grains of apatite (Fig. 10B). However, the chert matrix does not exhibit the same intergranular isopachous texture as the quartz in the Kipalu because it contains considerably more clay minerals along with more abundant carbonate rosettes (Fig. 10B-E). The carbonate is inferred from Raman spectra to be dolomitic in composition. It has  $\delta^{13}\text{C}_{\text{Carb}}$  and  $\delta^{18}\text{O}_{\text{SMOW}}$  values of -5.1 to -6.7‰ and +14.7 to +19.4‰, respectively (Table 2). Some carbonate rosettes have sub-

395 rhombohedral edges with circular to rhombohedral centres composed of chert and  
396 commonly contain nanoscopic inclusions of haematite.

397 OM is found as microscopic inclusions along the inner rim of some carbonate  
398 rosettes (Fig. 10D-E). The OM has strong and sharp D1-peaks around  $1352\text{ cm}^{-1}$ , less intense  
399 but sharp G-peaks around  $1598\text{ cm}^{-1}$ , and minor 2<sup>nd</sup> order peaks at  $2700\text{ cm}^{-1}$  and  $2950\text{ cm}^{-1}$   
400 (Fig. 10F). Crystallisation temperatures of  $310\text{--}317^\circ\text{C}$  were calculated (Table 3) and are  
401 consistent with metamorphism at the sub-greenschist facies. The TOC of the Akaitcho River  
402 GIF is low (0.03 to 0.04wt%), and it has  $\delta^{13}\text{C}_{\text{org}}$  values of  $-26.7$  to  $-28.0\text{‰}$  (Table 2). Rarely,  
403 some granules contain round haematite rosettes around  $10\text{--}30\text{ }\mu\text{m}$  in diameter with internal  
404 cores of dense haematite in their centre (Fig. 10H).

#### 405 **4.6 Petrology and geochemistry of the Frere granular iron formation**

406 The Frere GIF preserves variable mixtures of oxidised and reduced mineral  
407 assemblages in chert, ranging from OM- and magnetite-dominated (Fig. 3J-K) to haematite-  
408 dominated samples (Fig. 3L-N). Magnetite forms continuous layers and irregularly-shaped  
409 granules (Fig. 11A-B) in the Frere GIF, while haematite almost exclusively occurs as  
410 irregularly-shaped granules or disseminated throughout the chert as microscopic grains (Fig.  
411 11A). Some stilpnomelane granules contain inclusions of haematite, carbonate, apatite and  
412 OM (Fig. 11C). Detrital quartz grains are recognisable in chaotic layers of mixed magnetite  
413 and haematite-coated chamosite granules lying above magnetite layers (Fig. 11D). In OM-  
414 rich samples, granules are sub-spheroidal and dominantly composed of dense OM (Fig. 11F).  
415 Inside the granules quartz is coarser relative to the matrix, and some granules exhibit  
416 shrinkage cracks containing small amounts of chamosite (Fig. 11F). In more oxidised  
417 samples, haematite granules are composed of dense accumulations of nanoscopic

haematite inclusions in ankerite (Fig. 11G-H). Some granules also commonly have euhedral crystals of magnetite along the rims (Fig. 11H), although in the Frere, the magnetite crystals are much smaller compared to the Nastapoka and Biwabik granules. Haematite spheroids occur within some elongate millimetre-size granules along with filamentous structures (Fig. 11I).

The Raman spectra of OM in the Frere is defined by strong and sharp D1-peaks around  $1345\text{ cm}^{-1}$ , less intense but sharp G-peaks around  $1601\text{ cm}^{-1}$ , and minor 2<sup>nd</sup> order peaks around  $2690\text{ cm}^{-1}$  and  $2930\text{ cm}^{-1}$  (Fig. 11E). Crystallisation temperatures of  $293\text{--}334^{\circ}\text{C}$  were calculated (Table 3) and are consistent with metamorphism at the lower greenschist facies. The TOC for the iron-rich granular samples is in the same range as the other Palaeoproterozoic samples (0.02-0.03 wt%) with  $\delta^{13}\text{C}_{\text{org}}$  values of  $-23.8$  to  $-27.7\text{‰}$ , while the iron-poor sample has 1.56wt% TOC and a  $\delta^{13}\text{C}_{\text{org}}$  of  $-34.3\text{‰}$  (Table 2). Ankerite has highly variable  $\delta^{13}\text{C}_{\text{carb}}$  values between  $-3.9$  and  $-16.3\text{‰}$  along with  $\delta^{18}\text{O}_{\text{SMOW}}$  values from  $+14.1$  to  $+14.8\text{‰}$  (Table 2).

## 5.0 Discussion

### 5.1 The source of organic matter in Palaeoproterozoic granular iron formations

OM in GIFs is typically an accessory phase, typically around 0.01-0.1 wt% TOC, which has led some to suggest that microbial involvement in banded iron formation's deposition was negligible (Klein, 2005). However, even fossiliferous GIFs have exceptionally low TOC. For example, TOC for the stromatolitic Biwabik IFs is less than 0.04wt% (Table 2). While these OM concentrations are low, micro-Raman analyses show that the mineralogical and

structural characteristics of OM in these GIFs is consistent with metamorphism of syngenetic OM. The presence of syngenetic OM in the GIFs suggests living microorganisms or their decomposed remains, may have played a role in GIF formation during diagenesis.

The most common mode of occurrence for OM in the six worldwide late Palaeoproterozoic GIFs in this study, is in association with carbonate (Fig. 4B, 4E; 5G; 8H; 10E). Examples include 1) the occurrence of carbonate cementing detrital quartz grains in the Chuanlinggou GIF, 2) carbonate rhombohedral crystals growing between granules in the Nastapoka and Akaitcho River GIFs, 3) the common association of carbonate with OM and apatite in the Biwabik and Frere GIF. The general lack of carbonate veins demonstrate that carbonate in these GIFs formed during diagenesis and not from foreign fluids.

Non-biological sources of OM may be a possible source of carbon in GIFs. Siderite has been proposed to thermally decompose to form graphitic OM (McCollom, 2003; van Zuilen et al., 2003). Siderite does not begin to decompose until above 455°C (French and Rosenberg, 1965), however, and Raman spectra indicate that no OM in the samples in this study experienced temperatures above 330°C (Table 3). We conclude that decarbonation reactions were unlikely to have produced the observed OM and associated mineral assemblages in granules from all six late Palaeoproterozoic GIFs.

The next most common mineralogical association with OM is phyllosilicates and clay minerals (Fig. 4B; 5C; 6H; 8F). This mineral association is likely due to the ability of clays and phyllosilicate minerals to bind to and protect OM from degradation (Liu et al., 2013; McMahon et al., 2016). Finally, rare occurrences of OM are associated with haematite only in granules with haematite filaments from the Kipalu GIF (Fig. 9E). OM association with iron oxides is a dominant form of OM in soils and sediments, and is thought to be important in

the preservation of OM in modern geological settings (Lalonde et al., 2012). It follows that iron oxide-OM associations should be more common since nano-petrography of microfossils confirmed that iron-oxide is directly associated with OM in fossil cell walls (Wacey et al., 2014). Alternatively, Shapiro and Konhauser (2015) proposed that iron-oxide may replace OM and microfossil cell walls during diagenesis, which is a possible explanation for the relatively rare occurrence we found in this study.

The majority of the  $\delta^{13}\text{C}$  values of OM measured in the Palaeoproterozoic GIFs are between -26.0‰ to -29.9‰ (Table 2), averaging  $-27.8 \pm 0.2\text{‰}$ . These isotopic compositions are typical of autotrophic  $\text{CO}_2$ -fixation and fractionation by the RuBisCo enzyme (Schidlowski, 2001), and closely match the average for OM from the Paleoproterozoic period. These values are also similar to those isotopic compositions produced by circumneutral, iron-oxidising bacteria (Kennedy et al., 2010) or methane-producing Archaea (House et al., 2003). More negative  $\delta^{13}\text{C}$  values down to -36.1‰ and -34‰ measured for the Nastapoka and Frere GIF (Table 2) suggest recycling of OM, and a possible role from methanogenesis and oxidation. Methanogenesis is usually a final step in OM decay after electron acceptors have been exhausted. In GIFs the extensive oxidation of OM may result in the accumulation of  $\text{H}_2$  and  $\text{CO}_2$  providing sufficient sustenance for methanogens. Furthermore, there is no shortage of electron acceptors such as ferric iron in GIFs. These rather negative  $\delta^{13}\text{C}$  values are also consistent with the so-called Shunga-Francevillian Event during the late Palaeoproterozoic, which has also been related to massive oxidation of OM (Kump et al., 2011).

The diversity of OM crystallinity in the GIFs studied (Fig. 12) shows the minor differences in disorder that are likely due to small differences in diagenetic and

metamorphic conditions experienced by the six different GIFs studied. One exception is the Raman spectra of OM from the Mn-siderite matrix in the Chuanlinggou granular IF, which lacks a G-peak around  $1600\text{ cm}^{-1}$  suggesting this OM lacks stacked planar arrays of aromatic carbon. Instead, it shows a single, broad band peaking around  $1420\text{ cm}^{-1}$ , which may correspond to a combination of  $\text{CH}_2$  and  $\text{CH}_3$  scissor/ bend vibrations (Orendorff et al., 2002) and represent  $\text{sp}^3$ -bonded carbon. The presence of these two types of OM within the same sample suggests significant molecular differences between the two varieties of OM to account for their differing Raman spectra. Potentially, the broad peaked,  $\text{sp}^3$ -bonded carbon could be a younger, less degraded contaminant, however, this  $\text{sp}^3$ -bonded carbon does not cross-cut, or occur in granules. This would imply either preferential contamination localised to the matrix, or it is a primary phase, with a diagenetic control on the spatial distribution of this carbon.

The mineralogical occurrences of OM described above highlight the key mineralogical associations of syngenetic OM with apatite, carbonate, haematite, quartz and phyllosilicates in GIF. Such associations can be used to better constrain the origin and timing of emplacement of OM in older metamorphosed GIF and OM as a biosignature for early life.

### **5.2.1 Carbon-sulphur cycling in the Chuanlinggou pyrite-siderite granules**

The concentrically-laminated spheroidal pyrite grains along the rims of Chuanlinggou siderite granules exhibit similar morphologies to sulphide-rimmed carbonate granules in Jurassic sediments (Raiswell, 1976). Those Jurassic granules also have  $\delta^{13}\text{C}_{\text{carb}}$  values of -13 to -15‰ with spheroidal shaped pyrite rims around the edges of some granules (Coleman, 1993). In modern-day, coastal marshlands, siderite-iron sulphide granules form in reducing

509 zones about central cores that vary from detrital minerals to wood and metal fragments  
510 (Pye et al., 1990). Siderite inside these granules have  $\delta^{13}\text{C}_{\text{carb}}$  values as low as  
511 -11.8‰ suggestive of carbonate formation from the oxidation of isotopically light OM (Pye  
512 et al., 1990). The reduced mineral assemblages preserved in the Chuanlinggou siderite GIF  
513 suggests formation in an anoxic diagenetic environment. The presence of desiccated,  
514 rippled sandstones, with stromatolites and moderately sized rounded grains with detrital  
515 components, supports an intertidal setting. In these environments burial of OM from  
516 primary producers in the water column produced conditions suitable for heterotrophic  
517 metabolism at shallow sedimentary depths, in anoxic and organic-rich sediments. The  
518  $\delta^{13}\text{C}_{\text{carb}}$  values for siderite in the Chuanlinggou exhibit equally low compositions down to -  
519 9.3‰ (Table 2) indicative of siderite forming partly from OM oxidation.

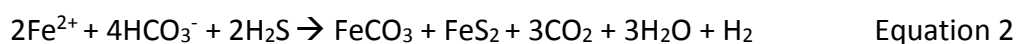
520 Siderite inside the Chuanlinggou granules exhibits an enrichment of Mg relative to  
521 the matrix, which conversely is enriched in Mn (Fig. 5I) (Table 1). This enrichment of Mg has  
522 been observed in other  $^{13}\text{C}$ -depleted carbonate granules containing framboidal pyrite that  
523 occur in landfill leachates (Feng and Chen, 2015). The Mg enrichment in these granules was  
524 suggested to be a favourable precipitate as a result of sulphate reduction and dissolved OM-  
525 Ca complexation, which binds Ca ions producing high Mg/ Ca ratios in pore waters (Feng and  
526 Chen, 2015). Additionally, extracellular polymeric substances (EPS) produced by sulphate-  
527 reducing bacteria (SRB) can also form Mg-carbonates (Bontognali et al., 2014). The  
528 production of EPS around detrital quartz grains may have seeped through fractures along  
529 the quartz grain surfaces and, then templated around quartz grains as a result of epitaxy  
530 processes resulting in the formation of OM rings within the quartz grain (Fig. 5E). Siderite-  
531 pyrite granules in Phanerozoic sediments are typically attributed to SRB (Coleman, 1993;



Coleman et al., 1993; Coleman and Raiswell, 1995; Pye et al., 1990; Raiswell, 1976). Similar, carbonate-pyrite granules have been recognised in Neoproterozoic phosphorites, many of which host microfossils (Xiao et al., 2010).

Granules built by SRB in modern environments (Preat et al., 2011) often contain detrital grains as substrates. Gliding masses of bacteria encircling the outermost margins accumulate EPS in the innermost layers around the grains (De Ridder and Brigmon, 2013). This utilisation of detrital grains by SRB may explain the occurrences of detrital quartz grains inside siderite granules in the Chuanlinggou GIF. Furthermore, these accumulating layers of EPS may bind clays and ferrihydrite leading to the formation of concentric equidistant layers around granules in the GIFs we studied (Fig. 4D-I; 5D; 6F). The granules in the Chuanlinggou exhibit many characteristic features of SRB activity, including isotopically light carbonate and OM, pyrite rims, Mg-enriched siderite, and detrital mineral cores. The following model is proposed for the formation of the Chuanlinggou pyrite-siderite granules (Fig. 13A-D):

- 1) Autotrophic activity in the water column produces significant quantities of OM in the sediments, followed by heterotrophic metabolism.
- 2) SRB colonize detrital quartz grains or clumps of OM within the anoxic sedimentary zone.
- 3) Sulphate reduction coupled to the oxidation of OM, produces bicarbonate and hydrogen sulphide according to the following chemical equation:  
$$\text{CH}_3\text{COOH} + \text{SO}_4^{2-} \rightarrow 2\text{HCO}_3^- + \text{H}_2\text{S} \quad \text{Equation 1}$$
- 4) Localised supersaturation of  $\text{HCO}_3^-$  promotes crystallization of coarse siderite within granules, as redox gradients create an outward diffusion of  $\text{HS}^-$  and inward migration of  $\text{Mg}^{2+}$  and  $\text{Fe}^{2+}$  to precipitate Mg-siderite granules.



5) Along the granule rims layered spheroidal pyrite forms as  $\text{H}_2\text{S}$  combines with  $\text{Fe}^{2+}$  (Fig. 5B). In some granules  $\text{H}_2\text{S}$  escapes, and others cations ( $\text{Mg}^{2+}$ ,  $\text{Al}^{2+}$ ) in the pore fluids were adsorbed to negatively charged EPS and OM along the granule margins to form clays (Fig. 5C).

In summary, localised activity of SRB within the Chuanlinggou sediments promoted the growth of siderite-pyrite granules during OM oxidation.

### **5.2.2 Biological activity in granules preserved as microbialites**

Finely layered, elongate, carbonaceous structures composed of haematite and carbonate are preserved in between detrital quartz grains in the Chuanlinggou sandstone (Fig. 4A), which is similar to microbial mats in other Precambrian siliciclastic sediments that also occur between quartz grains, and are composed of iron-oxides as well as isotopically-light OM (Heubeck, 2009; Noffke et al., 2003). The microbial mats in the Chuanlinggou occur along with OM, which is wrapped around quartz grains, and associated with apatite, illite and siderite (Fig. 4A-E). The concentricity of OM and haematite around these quartz grains is analogous to ooid granules, which also have concentric, spheroidal, and equidistant laminations of minerals. There is a distinctive lack of OM in the more ferruginous sandstones from the Chuanlinggou, but there is an abundance of stromatolites and ooid granules (Fig. 4H-I). Inside the laminae of these Chuanlinggou granules, six genera of bacteria have been reported (Dai, 2004), analogous to microfossils that occur in granules from the Frere GIF (Walter et al., 1976). Additionally, here we report haematitised filamentous microfossils in and around granules in the Kipalu GIF (Fig. 9B-D). In addition, it has been suggested that spheroidal haematite clusters that make up granules and layers in

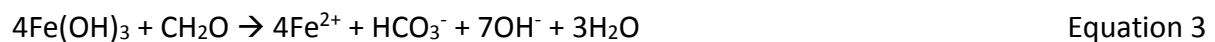
578 Palaeoproterozoic IF represent microfossils (Laberge, 1973). We found haematite spheroids  
579 from the Biwabik, Akaitcho River and Frere GIFs (Fig. 7C; 10H; 11I). Haematite spheroids  
580 form part or most of the haematite granules, and are rarely associated with tubular  
581 filaments (Fig. 11I). Almost identical spheroids are found in Phanerozoic jaspers (Grenne and  
582 Slack, 2003) and other Precambrian IF (Laberge, 1973). The style of haematite spheroid  
583 preservation is comparable to how bacteria are mineralised in modern iron-silica rich  
584 environments (Konhauser, 1998; Konhauser and Ferris, 1996). However, haematite  
585 spheroids in the GIFs studied lack association with biologically-relevant minerals such as  
586 OM, apatite and carbonate, therefore a biological origin is uncertain.

587         It is the recognition of microfossils in the laminae of ooid granules from other IFs  
588 that has led some to propose biological controls on the formation of ooid granules  
589 (Dahanayake et al., 1985; Dahanayake and Krumbein, 1986; Glasauer et al., 2013; Salama et  
590 al., 2013). Comparably, concentric layers of carbonate in modern-day granules of  
591 cyanobacterial colonies are a product of bacterial growth patterns (Brehm et al., 2006;  
592 Brehm et al., 2003). It has been suggested that ooid granules formed *in situ* (Dahanayake et  
593 al., 1985) and not from mechanical agitation. This interpretation is supported by the  
594 preservation of haematite-siderite concentric granules (Fig. 4D-E) and multiply bound  
595 granules in the GIFs here studied (Fig. 4I; 6A-B; 8C). These features demonstrate ooid  
596 granules were too fragile or unfavourably shaped to have formed via mechanical reworking  
597 in an agitated environment. Furthermore laboratory experiments have suggested that only  
598 2% of ooid granule growth may be achieved in an agitated environment, while the majority  
599 of growth is achieved in the subsurface (Davies et al., 1978). These same experiments could  
600 only form ooid granules in the presence of humic acids, especially those with carboxyl  
601 groups. It was noted the OM interacted with Ca and Mg to form concentric layers of

carbonate and OM (Davies et al., 1978). Similarly, observations have suggested concentric layer formation in modern-day freshwater ooid granules is controlled by permineralisation of EPS from photosynthetic bacteria (Pacton et al., 2012; Plee et al., 2008), which is also the mechanism put forward for the oldest known ooids from the Mesoarchean Pongola Supergroup, South Africa (Siahi et al., 2017). Like these examples, granules from the Biwabik GIF also have OM concentrated within concentric haematite and silicate layers (Fig. 6F-H). This is comparable to Eocene IFs, in which organic remains are preserved in the concentric and stromatolitic crusts around granules (Salama et al., 2013). Additionally, granules in the Chuanlinggou GIF also preserve OM in the peripheral, concentric layers (Fig. 4B; 4E). Microbialites occur as stromatolite-like columns protruding from the rims of some granules in the Biwabik GIF (Fig. 7C), which are similar to other Proterozoic sediments with stromatolite growths protruding from granules (Tang et al., 2015), as well as those from the Mesoarchean Pongola GIF (Smith et al., 2017). These provide further evidence for microbial involvement in haematite-magnetite layers around granules. Equally, in the Biwabik GIF, concretions can contain multiple concentrically-layered granules (Fig. 7A), in a similar manner to carbonate ooid granules coated by stromatolitic crusts in Phanerozoic sediments (Paul et al., 2011). Therefore, concentric iron-oxide layers about granules in GIFs likely formed via similar biological pathways involving bacterial growth about localised centres.

The granules of the Biwabik GIF contain carbonate and apatite with nanoscopic inclusions of isotopically-light OM (Fig. 6E; 7D-F). These mineralogical associations strongly suggest a biological influence on the formation of granules, whereby biomass would have decayed and oxidised inside granules to precipitate into carbonate and apatite. This is supported by low  $\delta^{13}\text{C}_{\text{Carb}}$  values of -12.3‰ in the Biwabik GIFs that indicate the assimilation of isotopically-light biomass into carbonate. The oxidation of biomass in the granules would

produce reduced mineral assemblages, such as magnetite rims around granules in the Biwabik and Nastapoka GIFs, analogous to the pyrite rimmed Chuanlinggou granules. Similarities in the structuring of granules in the Biwabik, Nastapoka and Chuanlinggou, suggest all these granules formed via a similar microbial pathway. Importantly it has been found that SRB utilise both sulphate and ferric iron for OM oxidation (Coleman et al., 1993). Therefore it is plausible that magnetite inside iron-oxide granules from the Biwabik and Nastapoka formations may represent microbial iron-reduction, as pyrite represents microbial sulphate reduction in the Chuanlinggou. Textural observations show that some magnetite-rimmed granules are subsequently encircled by concentric rims of haematite, both of these rims are cut by septarian cracks suggesting the rims had formed prior to dehydration and therefore, the magnetite rims had formed prior to metamorphism. If magnetite formed via the reduction of ferric iron with OM inside granules, the reaction may have proceeded as below:



The preservation of magnetite preferentially inside the granules suggests the intragranular portion of granules was relatively more anoxic compared to the haematite-rich, intergranular, diagenetic environment. Granules formed by SRB in modern marine environments are believed to maintain anaerobic conditions within granules (De Ridder and Brigmon, 2013). Gliding bacteria living in the outer layers of these granules produce extracellular polymeric substances which accumulates around the granule centres thereby forming concentric layers. These conditions provide suitable substrates for symbiotic growth of sulphur-reducing and sulphur-oxidising bacteria within and around the modern granules. Similarly, modern-day, deep-sea, Fe-Mn granules are believed to be structured by a host of

bacteria living inside and outside granules, comprising both metal oxidisers and reducers (Blothe et al., 2015; Yli-Hemminki et al., 2014). Based on the association of granules in the Biwabik (Fig. 1E-F) and Nastapoka GIFs with stromatolites, the outward, undulating and concave stromatolitic layering of some granule rims (Fig. 7C), and the average  $\delta^{13}\text{C}_{\text{org}}$  value of -27.8‰, it can be suggested that the microbial communities were dominated by phototrophic bacteria, such as cyanobacteria or photoferrotrophs. It has been suggested that ferruginous granules and stromatolites in the Biwabik, Nastapoka and Chuanlinggou GIFs are analogous to those from the Jurassic (Lazăr et al., 2012; Pr  at et al., 2000), which were formed by iron-oxidising bacteria living in dysoxic waters. Whether the ferric iron was aerobically or anaerobically oxidised by photoferrotrophs in the GIFs studied remains unclear. In brief, the concentric haematite-magnetite rims of granules in the Biwabik, Chuanlinggou and Nastapoka GIFs is best explained as controlled Fe-oxidation and deposition by bacteria living on or just under the sediment surface along the margins of granules. Inside these granules OM may have been utilised by heterotrophic bacteria to reduce the ferric iron to form magnetite rims.

In light of these comparable observations and the occurrence of 1) isotopically light OM and carbonate, 2) apatite with micron-size inclusions of OM inside magnetite rimmed granules, along with 3) peripheral concentric and stromatolitic layers of haematite, altogether suggest microorganisms contributed to the mineralogy and morphology of magnetite-haematite granules in late Palaeoproterozoic GIFs. Hence, the following model for magnetite-haematite granules is proposed (Fig. 13E-I):

- 1) Colonies of bacteria form rounded clumps in the water column and preferentially adsorb silica, iron and other cations. Continued production and accumulation of

extra-cellular polymeric substances into concentric layers efficiently trap ferric-oxyhydroxide and particulates to create organo-mineral spheroids.

2) A concentration of ferric iron and OM within and around the granules provides ideal conditions for iron reduction within the granules, some of which could have been non-biological. Hydro-magnetite is produced during these early diagenetic processes as a precursor to magnetite.

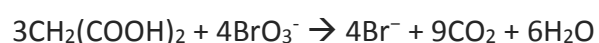
3) Fluid and gas content builds within the granules, fuelled by heterotrophic metabolisms and non-biological decomposition of OM. This leads to crystallisation of silica into large quartz crystals within the granules and minor carbonate formation around the granules.

4) Carbonate and apatite minerals form along with OM inside the granules as diagenetic processes liberate <sup>13</sup>C-depleted carbon and phosphorus from biomass.

5) Ensuing diagenesis dehydrates granules leading to septarian cracks, which cut through the previous layers of magnetite and haematite.

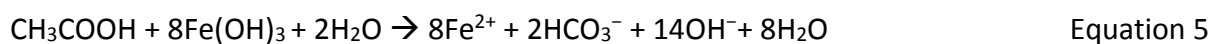
### **5.3 Diagenetic chemically-oscillating reactions and granule formation**

Chemically-oscillating reactions are examples of non-biological, non-equilibrium, oxidation-reduction reactions, which produce fractal patterns of curved equidistant laminations, which expand on timescales as short as a few minutes. These reactions usually include carboxylic acids, such as malonic acid in the case of the Belousov–Zhabotinsky (BZ) reaction, and oxidants like bromate and sulphate (Zaikin and Zhabotinsky, 1970). An equation can be written for this chemical reaction as follows:



Equation 4

In an early diagenetic environment, similar reactions may occur through the oxidation of organic acids from the breakdown of microbial OM (Papineau et al., 2017). In ferruginous environments, a likely reaction may proceed as the oxidation of acetic acid with ferrihydrite (Fig. 13J-M):



Alternatively, if sufficient sulphate was present in pore waters, then sulphate may spontaneously oxidise organic acids via the following equation:



In these equations, “CH<sub>3</sub>COOH” is used as generalisation for carboxyl groups in humic acids representing unmetamorphosed Palaeoproterozoic OM. Should these reactions produce concentrically-laminated patterns akin to those in the BZ reaction (Vanag and Epstein, 2003; Zaikin and Zhabotinsky, 1970), then it would be plausible to find these concentric patterns, and their reaction products in the geological record. It has been demonstrated experientially that non-biological oxidation of glucose (proxy for biological OM) with ferrihydrite (akin to Equation 2) produces rounded siderite structures (carbonate rosettes) similar to those in IFs (Kohler et al., 2013). Carbonate rosettes have also been recognised in the Gunflint and Brockman iron-formations (Kohler et al., 2013). Also, carbonate rosettes are found in the Kipalu, Akaitcho River and Frere GIFs (Fig. 9J; 10C), where they are formed of ankerite and dolomite respectively. In some cases, they contain nanoscopic inclusions of haematite and notably micron-sized OM (Fig. 10E). These observations suggest that the carbonate rosettes may have formed from oxidation of OM, possibly through chemically-oscillating reactions as was proposed in other granular chert and phosphatic stromatolites (Papineau et al., 2016). However, an alternative explanation for the formation of carbonate rosettes may be the



718 preferential dissolution of carbonate cores. During late diagenesis, significant chemical  
719 differences in the composition of the carbonate between the cores and rims of the crystal  
720 may lead to leaching of material from the core. For instance Fe-rich cores may be replaced  
721 by ankerite rims, during Mg replacement, or dolomitization type processes. However, the  
722  $\delta^{13}\text{C}_{\text{Carb}}$  values for these two GIFs show moderately depleted values from -5.1 to -9.0‰,  
723 supporting an origin for the carbonate rosettes involving the oxidation of OM and variable  
724 dilutions with seawater carbonate.

725         Granules in the Akaitcho River, Kipalu, and Frere GIF generally do not exhibit  
726 concentric morphologies of iron-oxide minerals and they often have irregular sub-spheroidal  
727 shapes. Diagenetic carbonate rosettes are common in the intergranular space of these GIFs,  
728 while granules in the Frere GIF often contain carbonate (Fig. 11C, H). Rarely within some  
729 granules, concentric haematite rosettes occur, such as in the Akaitcho River and Frere GIFs  
730 (Fig. 10H). Haematite rosettes are also common features of both modern-day Fe-Si vent  
731 deposits, and Precambrian and Phanerozoic IFs, but are debated as to what their origin may  
732 be. These rosettes have been interpreted as crystallisation effects of iron-silica gels (Grenne  
733 and Slack, 2003), diagenetic reaction products (Heaney and Veblen, 1991), clumping of  
734 particulates (Rasmussen et al., 2013), abiogenic precipitation (Sun et al., 2012) or  
735 microfossils (Laberge, 1973).

736         Isopachous quartz around granules in the Kipalu GIF suggest the granules were  
737 formed before silica infilled the pore space between granules cementing them together.  
738 Therefore if BZ-type reactions produced the granules, they should not have isopachous rims,  
739 as the granules would have formed *in-situ* before infilling of silica cement. This rational is  
740 reinforced by the presence of haematite microfossils which emanate from granules and are

741 preserved between them (Fig. 9C), demonstrating that the granules had formed before  
742 diagenesis allowing microbes to live between them.

743         Based on our data (Table 4), we propose that granules in the Biwabik, Nastapoka,  
744 and Chuanlinggou GIFs preserve reactants and products of possible chemically-oscillating  
745 reactions as well as some morphological features from such reactions. In the Biwabik and  
746 Nastapoka GIFs, a common feature of granules is reduced inner rims of magnetite, followed  
747 by more oxidised, haematitic, concentric rims (Fig. 6E; 7A; 8B). Similarly, in the  
748 Chuanlinggou GIF some siderite granules have reduced rims of pyrite (Fig. 5B), and  
749 carbonate-chamosite granules in the Frere GIF have crystals of magnetite which occur along  
750 the margins-. These reduced mineral rims may represent the outward diffusion of reaction  
751 products (i.e. magnetite, pyrite), as ferric iron and sulphate were reduced in reactions such  
752 as equations 5 and 6. OM-bearing apatite associated with carbonate inside roughly 20% of  
753 granules provides strong evidence for biomass oxidation inside granules (Fig. 6E; 7D-F). The  
754 coarser crystal size of quartz or siderite inside the granules, relative to their surrounding  
755 matrix (Fig. 5B; 6B; 7B; 8B; 9I; 11F), suggests longer growth times for the crystals, across  
756 different stages of diagenesis. Combined with the occurrence of septarian structures  
757 pinching toward granule centres, these features suggest the interiors of the granules were  
758 relatively fluid-rich before dehydration (Fig. 8B; 9H; 11F). A fluid-rich interior of the granules  
759 would also promote the preferential coarsening of crystals inside the granules prior to fluid  
760 escape, by allowing longer times for precipitation and crystallisation. Subsequent  
761 dehydration during diagenesis would incur shrinkage and septarian cracks. A fluid-rich  
762 interior of granules is consistent with a chemical-oscillatory model that would lead to the  
763 production of volatiles through the oxidation of OM releasing H<sub>2</sub>O and CO<sub>2</sub>.

Biogeochemical reactions may also be catalysed by heterotrophic microorganisms and have been proposed to account for the association of isotopically light carbonate and magnetite in Hamersley BIFs (Heimann et al., 2010). Experimental studies suggest abiotic and biotic iron-oxidation and reduction reactions proceed at almost indistinguishable rates (Ionescu et al., 2015), which makes separation of the two processes difficult. Mineralogical observations show that oxidation-reduction reactions occurred within granules and possibly led to curved equidistant laminations around them. Besides, while granules from the Akaitcho River, Kipalu and Frere GIFs lack sufficient products of these chemically-oscillating reactions, these other GIFs contain carbonate-haematite rosettes that also suggest a role for these reactions, although the different diagenetic conditions for these remain unclear and will be the subject of future investigations.

#### **5.4 Granules as a product of mechanical agitation?**

Evidence for the formation of GIFs from mechanical reworking has come from geological observations such as cross-bedding, detrital minerals, and other indicators of shallow-marine, high-energy settings, as well as the relatively small lensoidal outcrops of GIFs in comparison to the larger laminated silicate-BIFs in which they occur (Table 4). Additionally, the similarity in rare earth element profiles of micro-banded and overlying GIF units have been used to argue for one precipitation mechanism for both units, thereby leaving mechanical reworking as the cause for the physical differences (Beukes and Klein, 1990). Furthermore, in the Sokoman GIF in the Ferriman Group of Québec, Canada, the restricted occurrence of haematite microfossils inside granules and their truncation at granule boundaries has been used as evidence to suggest the granules are rounded detrital

grains (Knoll and Simonson, 1981). This mechanical agitation model generally implies that laminated silicate-BIF formed through precipitation in quiet and shallow water, subsequently siliceous-ferruginous gels were disrupted by traction currents generating siliceous-ferruginous granules, which were deposited in deeper water as lensoids in silicate-BIFs (Pufahl and Fralick, 2004). A stratified water column has been used to explain the observed differences in iron-oxide minerals preserved in GIFs (Akin et al., 2013; Pufahl and Fralick, 2004), whereby magnetite-rich iron formations were deposited in deeper, quiet waters and haematite-rich iron formations were deposited in shallow, well-mixed waters.

The selective distribution of magnetite and haematite in and around granules argues against physical reworking events (Table 4). Wave-action would deposit material randomly, instead of generating granules with internal magnetite rims surrounded by fine, concentric haematite layering (Fig. 6E, 7B, 8B). Additionally, mechanical abrasion would not concentrate carbonate, apatite and OM preferentially within granules (Fig. 6E, 7D-F). Also, multiple granules bound by fine, disseminated, concentric layers of nanoscopic haematite could not have formed in an energetic environment, as these delicate structures would easily be disrupted. However, granules from the Kipalu, Akaitcho River, and Frere GIFs do not exhibit magnetite rims or concentric layering (Fig. 9A; 10A; 11A); yet some carbonate-haematite granules in the Frere GIF do have euhedral magnetite grains along the margins (Fig. 11G-H). Importantly, these GIFs form jasper lenses in silicate BIF, in contrast to the more laterally continuous beds of the Biwabik GIFs. The mixture of detrital bearing minerals in the Kipalu, Akaitcho River and Frere GIFs supports mechanical re-working as a partial origin for the granule structures. The angular and structureless nature of some haematite granules in the Kipalu, Akaitcho River and Frere GIFs (Fig. 10A; 11A) therefore could be consistent with formation by either a mechanical abrasive model or via aggregation of silica

colloids (Stefurak et al., 2015). However, if silica aggregation was playing a role in granule formation, then the GIF should not form discrete lensoids in outcrop but rather form pervasive beds. Therefore, the lensoid outcrops of these GIFs, the shape and mineralogy of the granules and the presence of detrital phases like quartz clasts (Fig. 9G; 11D), round zircons (Fig. 4G) and Al-clays (Fig. 4B; 10B; 11C), suggest these GIFs may have been formed partly by the mechanical working of haematitic-siliceous gels on shallow seafloors (Table 4).

Chamosite and minnesotaite commonly occur inside granules in the Nastapoka and Frere GIFs with rims of haematite (Fig. 8D-F; 11A). Stilpnomelane granules occur without iron-oxide rims in other Frere samples (Fig. 11C), and OM granules occur with chamosite (Fig. 11F). These assemblages are consistent with the displacement and moulding of laminated Fe-silicate BIFs into granules composed of silicates and iron-oxide, or in the case of OM granules, the displacement of OM-rich silicate layers. These OM granules are similar to OM granules in dolomite, of the ca. 2,000 million year old Duck Creek carbonate, in which microfossils occur within and around granules (Knoll et al., 1988), like filaments in the Kipalu GIF. Relatedly, microfossils restricted to granules in the 1,900 million year old Sokoman GIF have been used to infer the granules formed prior to diagenesis (Knoll and Simonson, 1981). Such observations are consistent with mechanical reworking of fossiliferous sediments in some GIFs, but we conclude that biological processes and chemically-oscillating reactions during OM oxidation cannot be ignored and can contribute to the mineralogy, geochemical compositions, and morphology of granules.

## **6.0 Conclusions**

Angular and structureless haematite granules from lensoid outcrops of the Akaitcho River and Frere GIFs lack delicate morphologies, such as concentric mineral layering, and instead preserve detrital quartz and clay phases within and around granules. These observations suggest that mechanical sedimentation processes largely contributed to these particular GIFs (Table 4). The presence of  $^{13}\text{C}$ -depleted carbonate rosettes associated with OM in these GIFs suggest that diagenetic oxidation of OM occurred, possibly via chemically-oscillating reactions, which could have influenced granule morphology.

In contrast, granules from the Kipalu GIF often contain well preserved, well-rounded morphologies with homogeneous mineral assemblages along with intergranular  $^{13}\text{C}$ -depleted ankerite rosettes, suggesting that limited oxidation-reduction and BZ reactions occurred. The presence of isotopically light OM and microfossils within and around haematite Kipalu granules implies an active biological environment of deposition, perhaps with multiple generations of microbes inhabiting both the water column in which the granules formed, and in between granules after sedimentation. These granules, therefore, likely were formed prior to diagenesis possibly through a combination of mechanical working of haematitic-siliceous gels, and biologically-controlled iron precipitation that may have formed clumps of iron in the water column, along with limited BZ reactions that occurred during later diagenesis in the intergranular matrix.

In contrast, granules from the Chuanlinggou, Biwabik and Nastapoka GIFs preserve fine mineral laminations of haematite and magnetite, or siderite and pyrite, and internal mineral associations of OM, apatite and carbonate, unlikely to have been preserved or formed by mechanical reworking of ferruginous-siliceous gels (Table 4). Reworking of microbial mats may also create granules of OM and silicates (Fig. 11F). Deposition of

856 microbial mat “rip ups”, or colonies of microbes in the water column may mix with ferric  
857 iron and oxidise the OM in these mats. Oxidation of this OM may initiate chemically-  
858 oscillating reactions, creating spherical granules with reaction products dispersed as curved,  
859 equidistant laminations of haematite, magnetite and pyrite, along with apatite and  
860 isotopically light carbonate.

861         Alternatively, the mineralogical and structural characteristics of granules in the  
862 Chuanlinggou, Biwabik and Nastapoka GIFs and their associations with stromatolites and  
863 microfossils, support a more direct biological origin for the granules. We postulate that  
864 heterotrophic bacteria oxidised OM deposited in sediments coupled to ferric iron or  
865 sulphate reduction, producing magnetite or pyrite-rimmed granules respectively. In  
866 addition, symbiotic relationships with autotrophic microbes, such as cyanobacteria or  
867 photoferrotrophs, and iron- or sulphate-reducing bacteria, may have produced concentric  
868 haematite-magnetite layers around some granules by fixation of iron-oxyhydroxides during  
869 microbial growth cycles.

870         The presence of isotopically-light OM in association with <sup>13</sup>C-depleted carbonate,  
871 apatite and microfossils within and around some granules in six worldwide  
872 Palaeoproterozoic GIFs, indicate metabolic activities may play a key role either directly or  
873 indirectly in granule formation. Granules and rosettes, therefore, may be viewed as a  
874 biosignature of OM oxidation and have implications for other granules, including in  
875 Eoarchean iron formation from the Nuvvuagittuq Supracrustal Belt (Dodd et al., 2017),  
876 microfossil structures in Palaeoarchean black chert from the Apex Fm (Schopf and  
877 Kudryavtsev, 2012), microfossils within granules from the Doushantuo Fm (Qu et al., 2017;  
878 She et al., 2014), and haematite concretions on Mars (Ray et al., 2016).

879

## 880 Acknowledgements

881 M.S.D. and D.P. acknowledge support from UCL and the London centre for Nanotechnology,  
882 and a Doctoral training grant from Engineering and Physical Science Research Council, UK. D.P. and  
883 M. L. F. also thank the NASA Astrobiology Institute (grant # NNA04CC09A), the Carnegie Institution  
884 of Washington, the W. M. Keck Foundation (2007-6-29), and Carnegie of Canada for funding  
885 fieldwork in the Animikie, Akaitcho River, Nastapoka, Belcher Groups of Canada and the United  
886 States. The crew of S/V Kakivaq and Arctic Kingdom Polar Expeditions are thanked for logistical  
887 support in the Hudson Bay, and the Nunavut Research Institute, Qikiqtani Inuit Association, and CLEY  
888 are thanked for permits allowing scientific research on Inuit-owned lands. Z.S. and  
889 D.P. acknowledge financial support from the National Natural Science Foundation of China (grant #  
890 41272038) for field work in the Hutuo and Changcheng Groups of China. D.P. thanks the Geological  
891 Survey of Western Australia for access and support in the core library and W. Bleeker and D.A.D.  
892 Evans for enabling field work in the East Arm of the Great Slave Lake. We also thank J. Davy for  
893 assistance with sample preparation and SEM analyses, and W. Bleeker for discussions that improved  
894 this manuscript.

895

## 896 References

897 Akin, S. J., Pufahl, P. K., Hiatt, E. E., Pirajno, F., and Sheldon, N., 2013, Oxygenation of shallow marine  
898 environments and chemical sedimentation in Palaeoproterozoic peritidal settings: Frere  
899 Formation, Western Australia: *Sedimentology*, v. 60, no. 7, p. 1559-1582.  
900 Baadsgaard, H., Morton, R. D., and Olade, M. A. D., 1973, Rb-Sr isotopic age for the Precambrian  
901 lavas of the Seton formation, east arm of Great Slave lake, Northwest Territories: *Canadian*  
902 *Journal of Earth Sciences*, v. 10, no. 10, p. 1579-1582.  
903 Baragar, W. R. A., and Scoates, R. F. J., 1981, The Circum-Superior Belt: a Proterozoic plate margin?,  
904 in Kroner, A., ed., *Precambrian Plate Tectonics*: Amsterdam, Elsevier, p. 297-330.  
905 Beukes, N. J., and Cairncross, B., 1991, A lithostratigraphic-sedimentological reference profile for the  
906 late Archaean Mozaan group, Pongola sequence: application to sequence stratigraphy and  
907 correlation with the Witwatersrand supergroup: *South African Journal of Geology*, v. 94, p.  
908 44-69.



909 Beukes, N. J., and Klein, C., 1990, Geochemistry and sedimentology of a facies transition from  
 910 microbanded to granular ironformation in the early Proterozoic Transvaal supergroup, South  
 911 Africa: *Precambrian Research*, v. 47, p. 99-139.

912 Blothe, M., Węgorzewski, A., Müller, C., Simon, F., Kuhn, T., and Schippers, A., 2015, Manganese-  
 913 Cycling Microbial Communities Inside Deep-Sea Manganese Nodules: *Environ Sci Technol*, v.  
 914 49, no. 13, p. 7692-7700.

915 Bontognali, T. R. R., McKenzie, J. A., Warthmann, R. J., and Vasconcelos, C., 2014, Microbially  
 916 influenced formation of Mg-calcite and Ca-dolomite in the presence of exopolymeric  
 917 substances produced by sulphate-reducing bacteria: *Terra Nova*, v. 26, no. 1, p. 72-77.

918 Bowring, S. A., Schmus, W. R. V., and Hoffman, P. F., 1984, U-Pb zircon ages from Athapuscow  
 919 aulacogen, East arm of Great Slave Lake, N.W.T., Canada: *Canadian Journal of Earth  
 920 Sciences*, v. 21, p. 1315-1324.

921 Brehm, U., Krumbein, W., and Palinska, K., 2006, Biomicrospheres Generate Ooids in the Laboratory:  
 922 *Geomicrobiology Journal*, v. 23, no. 7, p. 545-550.

923 Brehm, U., Krumbein, W. E., and Palinska, K. A., 2003, Microbial spheres: a novel cyanobacterial-  
 924 diatom symbiosis: *Naturwissenschaften*, v. 90, no. 3, p. 136-140.

925 Chandler, F. W., 1981, The structure of the Richmond gulf graben and the geological environments  
 926 of lead-zinc mineralization and of iron-manganese formation in the Nastapoka Group,  
 927 Richmond gulf area, new Quebec - Northwest Territories: Geological Survey of Canada.

928 -, 1984, Metallogenesis of an early Proterozoic foreland sequence, eastern Hudson Bay, Canada:  
 929 *Journal of the Geological Society*, v. 141, p. 299-313.

930 Chandler, F. W., and Parrish, R. R., 1989, Age of the Richmond gulf group and implications for rifting  
 931 in the Trans-Hudson orogen, Canada: *Precambrian Research*, v. 44, p. 277-288.

932 Coleman, M. L., 1993, Microbial processes: Controls on the shape and composition of carbonate  
 933 concretions: *Marine Geology*, v. 113, p. 127-140.

934 Coleman, M. L., Hedrick, D. B., Lovley, D. R., White, D. C., and Pye, K., 1993, Reduction of Fe(III) in  
 935 sediments by sulphate-reducing bacteria *Nature*, v. 361, p. 436-438.

936 Coleman, M. L., and Raiswell, R., 1995, Source of carbonate and origin of zonation in pyritiferous  
 937 carbonate concretions: evaluation of a dynamic model *American Journal of Science*, v. 295,  
 938 p. 282-308.

939 Dahanayake, K., Gerdes, G., and Krumbein, W. E., 1985, Stromatolites, oncolites and oolites  
 940 biogenically formed in situ: *Naturwissenschaften*, v. 72, p. 513-518.

941 Dahanayake, K., and Krumbein, W. E., 1986, Microbial structures in oolitic iron formations:  
 942 *Mineralium Deposita*, v. 21, p. 85-94.

943 Dai, Y., 2004, Fossil bacteria in Xuanlong iron ore deposits of Hebei Province: *Science in China Series  
 944 D*, v. 47, no. 4, p. 347.

945 Davies, P. J., Bubela, B., and Ferguson, J., 1978, The formation of ooids: *Sedimentology*, v. 25, p. 703-  
 946 730.

947 De Ridder, C., and Brigmon, R. L., 2013, "Farming" of microbial mats in the hindgut of Echinoids, *in*  
 948 Krumbein, W. E., Paterson, D. M., and Zavarzin, G. A., eds., *Fossil and recent biofilms: A  
 949 natural history of life on Earth*: Netherlands, Springer Netherlands, p. 217-225.

950 Feng, J., and Chen, D., 2015, Characterization of authigenic carbonates from Huoshaogang landfill,  
 951 Guangzhou, China: implication for microbial metabolism: *Environmental Earth Sciences*, v.  
 952 74, no. 6, p. 4839-4851.

953 Fralick, P., Davis, D. W., and Kissin, S. A., 2002, The age of the Gunflint Formation, Ontario, Canada:  
 954 single zircon U-Pb age determinations from reworked volcanic ash: *Canadian Journal of  
 955 Earth Sciences*, v. 39, p. 1085-1091.

956 French, B. M., and Rosenberg, P. E., 1965, Siderite (FeCO<sub>3</sub>): thermal decomposition in equilibrium  
 957 with graphite: *Science*, v. 147, no. 3663, p. 1283-1284.

958 Gao, L. Z., Zhang, C. H., Liu, P. J., Ding, X. Z., Wang, Z. Q., and Zhang, Y. J., 2009, Recognition of meso-  
959 And neoproterozoic stratigraphic framework in North and South China: *Acta Geoscientica*  
960 *Sinica*, v. 30, no. 4, p. 433-446.

961 Glasauer, S., Mattes, A., and Gehring, A., 2013, Constraints on the Preservation of Ferriferous  
962 Microfossils: *Geomicrobiology Journal*, v. 30, no. 6, p. 479-489.

963 Grenne, T., and Slack, J. F., 2003, Bedded jaspers of the Ordovician Løkken ophiolite, Norway:  
964 seafloor deposition and diagenetic maturation of hydrothermal plume-derived silica-iron  
965 gels: *Mineralium Deposita*, v. 38, no. 5, p. 625-639.

966 Gruner, J. W., 1924, Contributions to the geology of the Mesabi Range: The University of Minnesota.

967 Hamilton, M. A., Buchan, K. L., Ernst, R. E., and Scott, G. M., 2009, Widespread and short-lived 1870  
968 Ma mafic magmatism along the northern Superior craton margin, 2009 Joint Assembly:  
969 Toronto, Ontario, Canada.

970 Heaney, P. J., and Veblen, D. R., 1991, An examination of spherulitic dubiomicrofossils in  
971 Precambrian banded iron formations using the transmission electron microscope:  
972 *Precambrian Research*, v. 49, p. 355-372.

973 Heimann, A., Johnson, C. M., Beard, B. L., Valley, J. W., Roden, E. E., Spicuzza, M. J., and Beukes, N. J.,  
974 2010, Fe, C, and O isotope compositions of banded iron formation carbonates demonstrate a  
975 major role for dissimilatory iron reduction in ~2.5 Ga marine environments: *Earth and*  
976 *Planetary Science Letters*, v. 294, p. 8-18.

977 Heubeck, C., 2009, An early ecosystem of Archean tidal microbial mats (Moodies Group, South  
978 Africa, ca. 3.2 Ga): *Geology*, v. 37, no. 10, p. 931-934.

979 Hoffman, P. F., 1968, Stratigraphy of the lower Proterozoic (aphebian), Great Slave supergroup, east  
980 arm of Great Slave lake, district of Mackenzie, *in* Department of energy, m. a. r., ed.: Ottawa,  
981 Geological Survey of Canada.

982 House, C. H., Schopf, J. W., and Stetter, K. O., 2003, Carbon isotopic fractionation by Archaeans and  
983 other thermophilic prokaryotes: *Organic Geochemistry*, v. 34, no. 3, p. 345-356.

984 Ionescu, D., Heim, C., Polerecky, L., Thiel, V., and de Beer, D., 2015, Biotic and abiotic oxidation and  
985 reduction of iron at circumneutral pH are inseparable processes under natural conditions:  
986 *Geomicrobiology Journal*, v. 32, no. 3-4, p. 221-230.

987 Kennedy, C. B., Gault, A. G., Fortin, D., Clark, I. D., Pedersen, K., Scott, S. D., and Ferris, F. G., 2010,  
988 Carbon isotope fractionation by circumneutral iron-oxidizing bacteria: *Geology*, v. 38, no. 12,  
989 p. 1087-1090.

990 Klein, C., 2005, Some Precambrian banded iron-formations (BIFs) from around the world: Their age,  
991 geologic setting, mineralogy, metamorphism, geochemistry, and origins: *American*  
992 *Mineralogist*, v. 90, no. 10, p. 1473-1499.

993 Knoll, A. H., and Simonson, B. M., 1981, Early Proterozoic microfossils and penecontemporaneous  
994 quartz cementation in the Sokoman iron formation, Canada: *Science*, v. 211, p. 478-480.

995 Knoll, A. H., Strother, P., and Rossi, S., 1988, Distribution and diagenesis of microfossils from the  
996 lower Proterozoic duck creek dolomite, Western Australia: *Precambrian Research*, v. 38, p.  
997 257-279.

998 Kohler, I., Konhauser, K. O., Papineau, D., Bekker, A., and Kappler, A., 2013, Biological carbon  
999 precursor to diagenetic siderite with spherical structures in iron formations: *Nat Commun*, v.  
1000 4, p. 1741.

1001 Konhauser, K. O., 1998, Diversity of bacterial iron mineralization: *Earth-Science Reviews*, v. 43, no. 3-  
1002 4, p. 91-121.

1003 Konhauser, K. O., and Ferris, F. G., 1996, Diversity of iron and silica precipitation by microbial mats in  
1004 hydrothermal waters, Iceland: Implications for Precambrian iron formations: *Geology*, v. 24,  
1005 no. 4, p. 323-326.

1006 Kouketsu, Y., Mizukami, T., Mori, H., Endo, S., Aoya, M., Hara, H., Nakamura, D., and Wallis, S., 2014,  
1007 A new approach to develop the Raman carbonaceous material geothermometer for low-  
1008 grade metamorphism using peak width: *Island Arc*, v. 23, no. 1, p. 33-50.

- Kump, L. R., Junium, C. K., Arthur, M. A., Brasier, A. T., Fallick, A. E., Melezhik, V., Lepland, A., Crne, A. E., and Luo, G., 2011, Isotopic evidence for massive oxidation of organic matter following the Great Oxidation Event: *Science*, v. 334, p. 1694-1696.
- Kusky, T. M., and Li, J., 2003, Paleoproterozoic tectonic evolution of the North China Craton: *Journal of Asian Earth Sciences*, v. 22, no. 4, p. 383-397.
- Laberge, G. L., 1973, Possible Biological Origin of Precambrian Iron-Formations: *Economic Geology*, v. 68, no. 7, p. 1098-1109.
- Lahfid, A., Beyssac, O., Deville, E., Negro, F., Chopin, C., and Goffé, B., 2010, Evolution of the Raman spectrum of carbonaceous material in low-grade metasediments of the Glarus Alps (Switzerland): *Terra Nova*, v. 22, no. 5, p. 354-360.
- Lalonde, K., Mucci, A., Ouellet, A., and Gelin, Y., 2012, Preservation of organic matter in sediments promoted by iron: *Nature*, v. 483, no. 7388, p. 198-200.
- Lascelles, D. F., 2007, Black smokers and density currents: A uniformitarian model for the genesis of banded iron-formations: *Ore Geology Reviews*, v. 32, no. 1-2, p. 381-411.
- Lazăr, I., Grădinaru, M., and Petrescu, L., 2012, Ferruginous microstromatolites related to Middle Jurassic condensed sequences and hardgrounds (Bucegi Mountains, Southern Carpathians, Romania): *Facies*, v. 59, no. 2, p. 359-390.
- Li, H. K., Su, W. B., Zhou, H. Y., Geng, J. Z., Xiang, Z. Q., Cui, Y. R., Liu, W. C., and Lu, S. N., 2011, The base age of the Changchengian System at the northern North China Craton should be younger than 1670 Ma: constraints from zircon U–Pb LA-MC-ICPMS dating of a granite-porphry dike: *Earth Science Frontiers* v. 18, p. 108-120.
- Liu, H., Yuan, P., Qin, Z., Liu, D., Tan, D., Zhu, J., and He, H., 2013, Thermal degradation of organic matter in the interlayer clay–organic complex: A TG-FTIR study on a montmorillonite/12-aminolauric acid system: *Applied Clay Science*, v. 80–81, p. 398-406.
- Lougheed, M. S., 1983, Origin of Precambrian iron-formations in the Lake Superior region: *Geological Society of America Bulletin*, v. 94, p. 325-340.
- Luo, G., Junium, C. K., Kump, L. R., Huang, J., Li, C., Feng, Q., Shi, X., Bai, X., and Xie, S., 2014, Shallow stratification prevailed for ~1700 to ~1300 Ma ocean: Evidence from organic carbon isotopes in the North China Craton: *Earth and Planetary Science Letters*, v. 400, p. 219-232.
- McCullom, T. M., 2003, Formation of meteorite hydrocarbons from thermal decomposition of siderite (FeCO<sub>3</sub>): *Geochimica Et Cosmochimica Acta*, v. 67, p. 311-317.
- McMahon, S., Anderson, R. P., Saupe, E. E., and Briggs, D. E. G., 2016, Experimental evidence that clay inhibits bacterial decomposers: Implications for preservation of organic fossils: *Geology*, v. 44, no. 10, p. 867-870.
- Neuendorf, K. K. E., Mehl, J. P., and Jackson, J. A., 2005, Glossary of geology, Alexandria, Virginia, American geological institute.
- Noffke, N., Hazen, R. M., and Nhlenk, N., 2003, Earth's earliest microbial mats in a siliciclastic marine environment (2.9 Ga Mozaan Group, South Africa): *Geology*, v. 31, no. 8, p. 673-676.
- Ojakangas, R. W., 1983, Tidal deposits in the early Proterozoic basin of the Lake Superior region—the Palms and the Pokegama Formations: Evidence for subtidal-shelf deposition of Superior-type banded iron-formation, *Early Proterozoic geology of the Great Lakes region*, Volume 160, Geological Society of America Memoir, p. 49-66.
- Orendorff, C. J., Ducey, M. W., and Pemberton, J. E., 2002, Quantitative Correlation of Raman Spectral Indicators in Determining Conformational Order in Alkyl Chains: *The Journal of Physical Chemistry A*, v. 106, no. 30, p. 6991-6998.
- Pacton, M., Ariztegui, D., Wacey, D., Kilburn, M. R., Rollion-Bard, C., Farah, R., and Vasconcelos, C., 2012, Going nano: A new step toward understanding the processes governing freshwater ooid formation: *Geology*, v. 40, no. 6, p. 547-550.
- Papineau, D., De Gregorio, B., Fearn, S., Kilcoyne, D., McMahon, G., Purohit, R., and Fogel, M., 2016, Nanoscale petrographic and geochemical insights on the origin of the Palaeoproterozoic stromatolitic phosphorites from Aravalli Supergroup, India: *Geobiology*, v. 14, no. 1, p. 3-32.

- Papineau, D., She, Z., and Dodd, M. S., 2017, Chemically-oscillating reactions during the diagenetic oxidation of organic matter and in the formation of granules in late Palaeoproterozoic chert from Lake Superior: *Chemical Geology*, v. 470, p. 33-54.
- Paul, J., Peryt, T. M., and Burne, R. V., 2011, Kalkowsky's stromatolites and oolites (Lower Buntsandstein, Northern Germany), *in* Reitner, J., Queric, N., and Arp, G., eds., *Advances in stromatolite geobiology*: Berlin Springer Berlin Heidelberg, p. 13-28.
- Pickard, A., 2003, SHRIMP U–Pb zircon ages for the Palaeoproterozoic Kuruman Iron Formation, Northern Cape Province, South Africa: evidence for simultaneous BIF deposition on Kaapvaal and Pilbara Cratons: *Precambrian Research*, v. 125, no. 3-4, p. 275-315.
- Pirajno, F., Hocking, R. M., Reddy, S. M., and Jones, A. J., 2009, A review of the geology and geodynamic evolution of the Palaeoproterozoic Earaheedy Basin, Western Australia: *Earth-Science Reviews*, v. 94, no. 1-4, p. 39-77.
- Plee, K., Ariztegui, D., Martini, R., and Davaud, E., 2008, Unravelling the microbial role in ooid formation - results of an in situ experiment in modern freshwater Lake Geneva in Switzerland: *Geobiology*, v. 6, no. 4, p. 341-350.
- Preat, A., De Jong, J. T. M., De Ridder, C., and Gillan, D. C., 2011, Possible Fe Isotope Fractionation During Microbiological Processing in Ancient and Modern Marine Environments, *in* Tewari, V., and Seckbach, J., eds., *STROMATOLITES: Interaction of Microbes with Sediments*, Volume 18: Netherlands, Springer, p. 651-673.
- Préat, A., Mamet, B., Ridder, C. D., Boulvain, F., and Gillan, D., 2000, Iron bacterial and fungal mats, Bajocian stratotype (Mid-Jurassic, northern Normandy, France): *Sedimentary Geology*, v. 137, p. 107-126.
- Pufahl, P. K., and Fralick, P. W., 2004, Depositional controls on Palaeoproterozoic iron formation accumulation, Gogebic Range, Lake Superior region, USA: *Sedimentology*, v. 51, no. 4, p. 791-808.
- Pye, K., Dickson, J. A. D., Schiavon, N., Coleman, M. L., and Cox, M., 1990, Formation of siderite-Mg-calcite-iron sulphide concretions in intertidal marsh and sandflat sediments, north Norfolk, England: *Sedimentary*, v. 37, p. 325-343.
- Qu, Y., Wang, J., Xiao, S., Whitehouse, M., Engdahl, A., Wang, G., and McLoughlin, N., 2017, Carbonaceous biosignatures of diverse chemotrophic microbial communities from chert nodules of the Ediacaran Doushantuo Formation: *Precambrian Research*, v. 290, p. 184-196.
- Rahl, J., Anderson, K., Brandon, M., and Fassoulas, C., 2005, Raman spectroscopic carbonaceous material thermometry of low-grade metamorphic rocks: Calibration and application to tectonic exhumation in Crete, Greece: *Earth and Planetary Science Letters*, v. 240, no. 2, p. 339-354.
- Raiswell, R., 1976, The microbiological formation of carbonate concretions in the upper Lias of NE England: *Chemical Geology*, v. 18, p. 227-244.
- Rasmussen, B., Fletcher, I. R., Bekker, A., Muhling, J. R., Gregory, C. J., and Thorne, A. M., 2012, Deposition of 1.88-billion-year-old iron formations as a consequence of rapid crustal growth: *Nature*, v. 484, no. 7395, p. 498-501.
- Rasmussen, B., Meier, D. B., Krapez, B., and Muhling, J. R., 2013, Iron silicate microgranules as precursor sediments to 2.5-billion-year-old banded iron formations: *Geology*, v. 41, no. 4, p. 435-438.
- Ray, D., Shukla, A. D., and Chandra, U., 2016, Mineralogy, geochemistry and Mossbauer spectroscopy of iron concretions from Jurassic formation of Kutch, India: more insights in to the depositional history and implications to Martian "blueberries", 47th Lunar and Planetary Science Conference: Houston, Texas.
- Roscoe, S. M., Gandhi, S. S., Charbonneau, B. W., Maurice, Y. T., and Gibb, R. A., 1987, Mineral resource assessment of the area in the east arm (Great Slave lake) and Artillery lake region N.W.T., Proposed as a national park *in* Department of Energy, M. a. R. G. S. o. C., ed.: Ottawa, Geological Survey of Canada, p. 10-18.

1111 Salama, W., El Aref, M. M., and Gaupp, R., 2013, Mineral evolution and processes of ferruginous  
1112 microbialite accretion - an example from the Middle Eocene stromatolitic and ooidal  
1113 ironstones of the Bahariya Depression, Western Desert, Egypt: *Geobiology*, v. 11, no. 1, p.  
1114 15-28.

1115 Schidlowski, M., 2001, Carbon isotopes as biogeochemical recorders of life over 3.8 Ga of Earth  
1116 history: evolution of a concept: *Geochimica Et Cosmochimica Acta*, v. 106, p. 117-134.

1117 Schneider, D. A., Bickford, M. E., Cannon, W. F., Schulz, K. J., and Hamilton, M. A., 2002, Age of  
1118 volcanic rocks and syndepositional iron formations, Marquette Range Supergroup:  
1119 implications for the tectonic setting of Paleoproterozoic iron formations of the Lake Superior  
1120 region: *Canadian Journal of Earth Sciences*, v. 39, no. 6, p. 999-1012.

1121 Schopf, J. W., and Kudryavtsev, A. B., 2012, Biogenicity of Earth's earliest fossils: A resolution of the  
1122 controversy: *Gondwana Research*, v. 22, no. 3-4, p. 761-771.

1123 Schulz, K. J., and Cannon, W. F., 2007, The Penokean orogeny in the Lake Superior region:  
1124 Precambrian Research, v. 157, no. 1-4, p. 4-25.

1125 Shapiro, R. S., and Konhauser, K. O., 2015, Hematite-coated microfossils: primary ecological  
1126 fingerprint or taphonomic oddity of the Paleoproterozoic?: *Geobiology*, v. 13, no. 3, p. 209-  
1127 224.

1128 She, Z.-B., Strother, P., and Papineau, D., 2014, Terminal Proterozoic cyanobacterial blooms and  
1129 phosphogenesis documented by the Doushantuo granular phosphorites II: Microbial  
1130 diversity and C isotopes: *Precambrian Research*, v. 251, p. 62-79.

1131 She, Z., Strother, P., McMahon, G., Nittler, L. R., Wang, J., Zhang, J., Sang, L., Ma, C., and Papineau,  
1132 D., 2013, Terminal Proterozoic cyanobacterial blooms and phosphogenesis documented by  
1133 the Doushantuo granular phosphorites I: In situ micro-analysis of textures and composition:  
1134 *Precambrian Research*, v. 235, p. 20-35.

1135 Siah, M., Hofmann, A., Master, S., Mueller, C. W., and Gerdes, A., 2017, Carbonate ooids of the  
1136 Mesoarchaeon Pongola Supergroup, South Africa: *Geobiology*.

1137 Simonson, B. M., 2003, Origin and evolution of large Precambrian iron formations., *in* Chan, M. A.,  
1138 and Archer, A. W., eds., *Extreme Depositional Environments: Mega End Members in*  
1139 *Geologic Time*, Volume 370, GSA Spec. Pap, p. 231-244.

1140 Smith, A. J. B., Beukes, N. J., Gutzmer, J., Johnson, C. M., and Czaja, A. D., 2017, Iron isotope  
1141 fractionation in stromatolitic oncoidal iron formation, Mesoarchean Witwatersrand-Mozaan  
1142 Basin, South Africa: *Geobiology*, v. 76, p. 2384.

1143 Stefurak, E. J. T., Lowe, D. R., Zentner, D., and Fischer, W. W., 2015, Sedimentology and geochemistry  
1144 of Archean silica granules: *Geological Society of America Bulletin*, p. B31181.31181.

1145 Sun, Z., Zhou, H., Glasby, G. P., Sun, Z., Yang, Q., Yin, X., and Li, J., 2012, Mineralogical  
1146 characterization and formation of Fe-Si oxyhydroxide deposits from modern seafloor  
1147 hydrothermal vents: *American Mineralogist*, v. 98, no. 1, p. 85-97.

1148 Tang, D., Shi, X., Shi, Q., Wu, J., Song, G., and Jiang, G., 2015, Organomineralization in  
1149 Mesoproterozoic giant ooids: *Journal of Asian Earth Sciences*, v. 107, p. 195-211.

1150 Tobin, K. J., 1990, The paleoecology and significance of the Gunflint-type microbial assemblages  
1151 from the Frere Formation (Early Proterozoic), Nabberu Basin, Western Australia.:  
1152 *Precambrian Research*, v. 47, p. 71-81.

1153 Trendall, A. F., 2002, The significance of iron-formation in the Precambrian stratigraphic record, *in*  
1154 Altermann, W., and Corcoran, P. L., eds., *Precambrian Sedimentary Environments: A Modern*  
1155 *Approach to Ancient Depositional Systems*, International Association of Sedimentologists.

1156 van Zuilen, M. A., Lepland, A., Teranes, J., Finarelli, J., Wahlen, M., and Arrhenius, G., 2003, Graphite  
1157 and carbonates in the 3.8 Ga old Isua Supracrustal Belt, southern West Greenland:  
1158 *Precambrian Research*, v. 126, no. 3-4, p. 331-348.

1159 Vanag, V. K., and Epstein, I. R., 2003, From the Cover: Segmented spiral waves in a reaction-diffusion  
1160 system: *Proc Natl Acad Sci U S A*, v. 100, no. 25, p. 14635-14638.

1161 Wacey, D., Saunders, M., Roberts, M., Menon, S., Green, L., Kong, C., Culwick, T., Strother, P., and  
 1162 Brasier, M. D., 2014, Enhanced cellular preservation by clay minerals in 1 billion-year-old  
 1163 lakes: *Sci Rep*, v. 4, p. 5841.  
 1164 Walter, M. R., Goode, A. D. T., and Hall, W. D. M., 1976, Microfossils from a newly discovered  
 1165 Precambrian stromatolitic iron formation in Western Australia *Nature*, v. 261, p. 221-223.  
 1166 Xiao, S., Schiffbauer, J. D., McFadden, K. A., and Hunter, J., 2010, Petrographic and SIMS pyrite sulfur  
 1167 isotope analyses of Ediacaran chert nodules: Implications for microbial processes in pyrite  
 1168 rim formation, silicification, and exceptional fossil preservation: *Earth and Planetary Science*  
 1169 *Letters*, v. 297, no. 3-4, p. 481-495.  
 1170 Yli-Hemminki, P., Jørgensen, K. S., and Lehtoranta, J., 2014, Iron–Manganese Concretions Sustaining  
 1171 Microbial Life in the Baltic Sea: The Structure of the Bacterial Community and Enrichments in  
 1172 Metal-Oxidizing Conditions: *Geomicrobiology Journal*, v. 31, no. 4, p. 263-275.  
 1173 Zaikin, A. N., and Zhabotinsky, A. M., 1970, Concentration wave propagation in two-dimensional  
 1174 liquid-phase self-oscillating system: *Nature*, v. 225, p. 535-537.

1175

1176



**Figure 1**

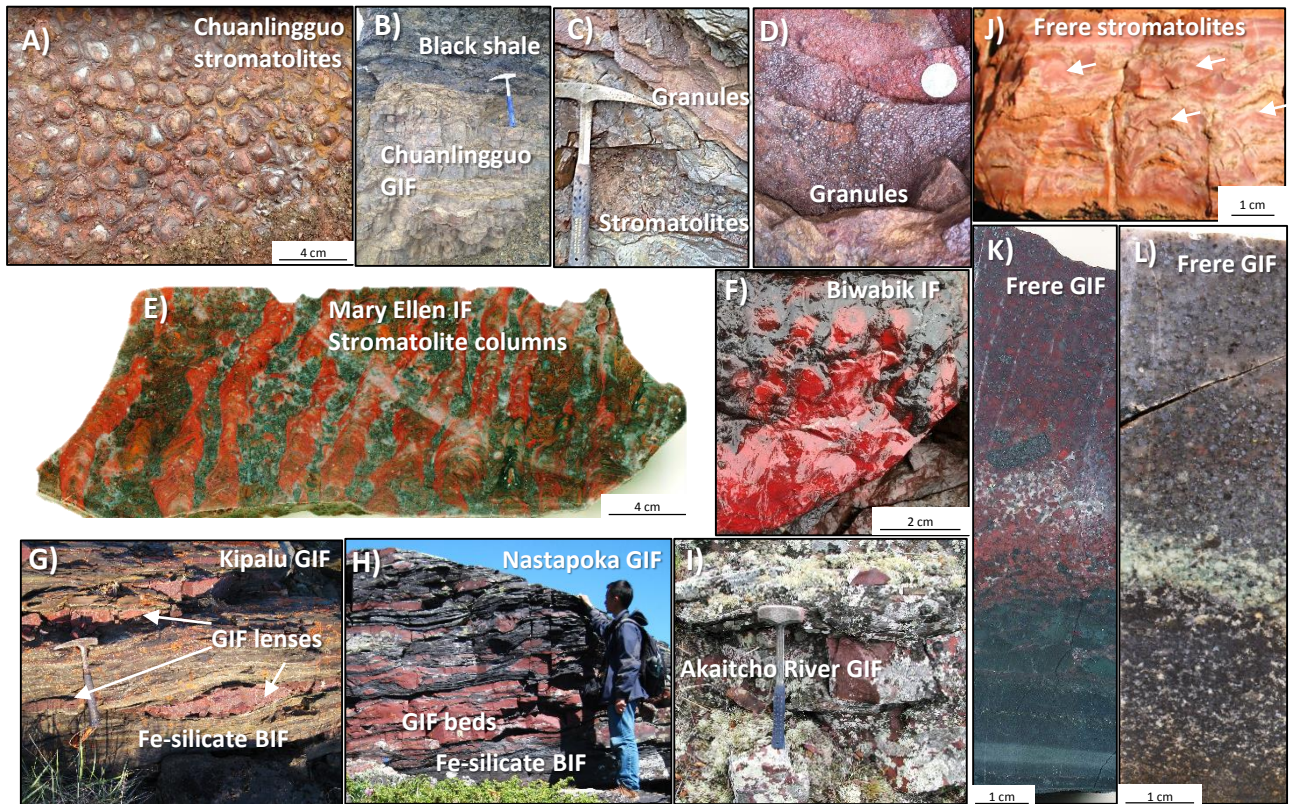


Figure 1. Field and sample images of iron formation (IF) in this study. A) Field outcrop of columnar stromatolites from the chuanlingguo IF. B) Conformable contact between black shale and chuanlingguo IF (hammer 50cm long). C) Field outcrop of stromatolite and granule-bearing beds in the chuanlingguo IF. D) Magnified image of chuanlingguo granule bed. E) Slab of stromatolitic IF from the Mary Ellen mine in the Animikie group, Biwabik Fm. F) Field outcrop of Stromatolites in the Biwabik IF. G) Field outcrops of the Kipalu GIF occurring as lenses and beds in Fe-silicate BIF. H) Field outcrops of the Nastapoka GIF occurring as lenses and pinching and swelling structures in Fe-silicate BIF. I) Outcrop of lenses of Akaitcho River GIF from the Great Slave Supergroup, J) Putative stromatolites in the Frere jasper with white arrows showing centimetre-size non-branching columns, K-L) TDH26-series core samples of the Frere GIF showing two samples with high and low haematite content K) TDH26-247.95 and L) TDH26-262.4

Figure 2

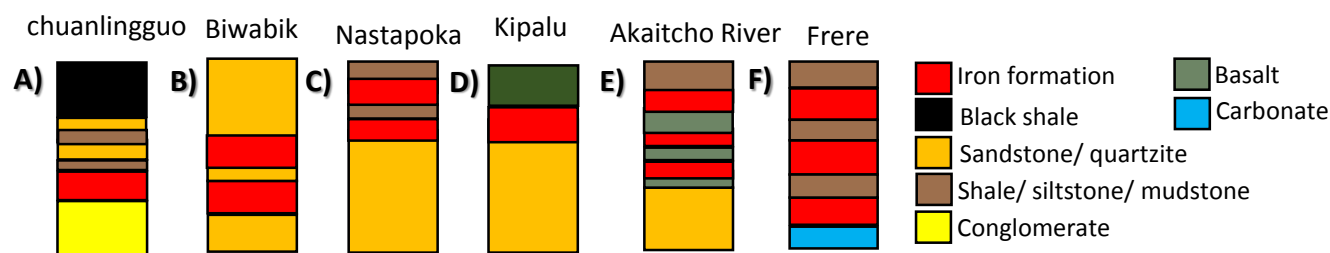


Figure 2. Simplified stratigraphic columns of the IF samples studied, showing relative bed thickness not to scale. Colours represents the main rock types for each of these IF. The A) Chuanlingguo IF in the Changcheng Group (Luo et al., 2014), B) Biwabik IF in the Animike Group (Ojakangas et al., 2011), C) Nastapoka IF in the Nastapoka Group and D) Kipalu IF in the Belcher Group (Chandler, 1984), E) Akaitcho River IF in the Great Slave Supergroup (Roscoe et al., 1987; Hoffman, 1969) and F) Frere IF in the Eeraheady Group (Pirajno et al., 2009). Iron formation thicknesses variable, columns not to scale.



# Figure 3

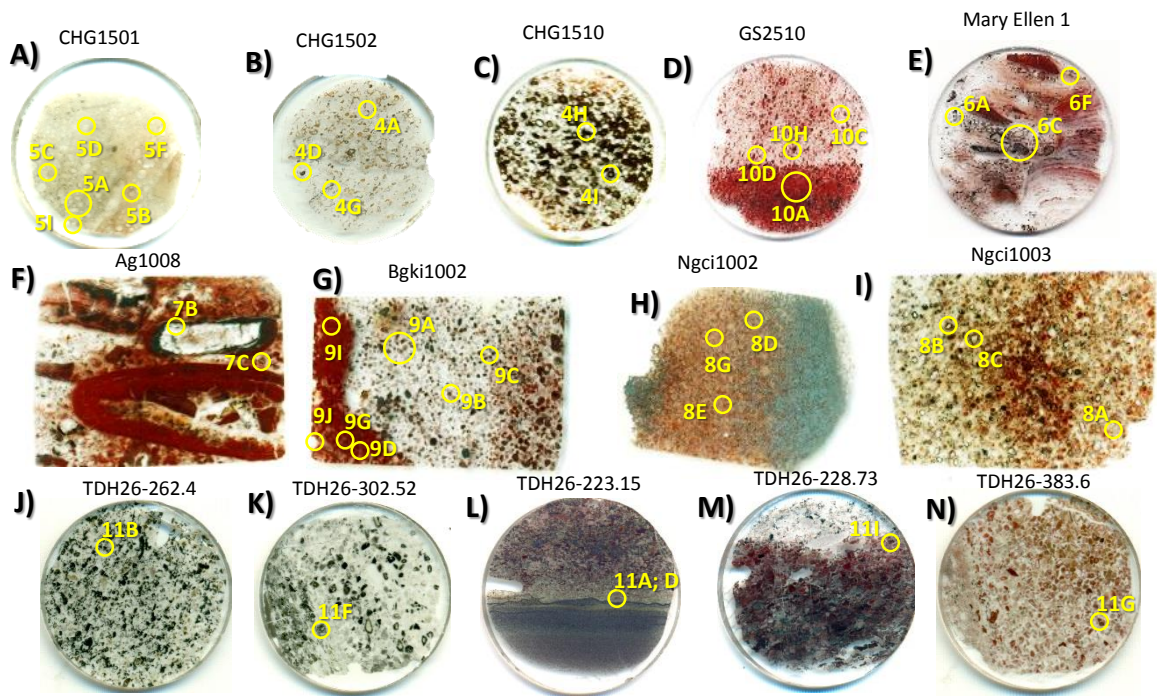


Figure 3. Thin sections (TS) of the samples studied in this work. A) TS of Chuanlingguo siderite GIF, B-C) TS images of iron-oxide Chuanlingguo GIF, D) TS scan of Akaitcho River GIF, E) TS image of Biwabik stromatolitic GIF from Mary Ellen mine, F) TS image of Biwabik IF from Thunderbird mine, G) TS image of Kipalu GIF from Flaherty Island, H-I) TS image of Nastapoka GIF from Clark Island, J-N) TS images of Frere GIFs from drill core TDH26 with depth in meters. All images presented in this study are located by their figure panel numbers written in yellow. All circular TS are 2.5cm in diameter, whereas rectangular sections are 3x2cm.

**Figure 4**

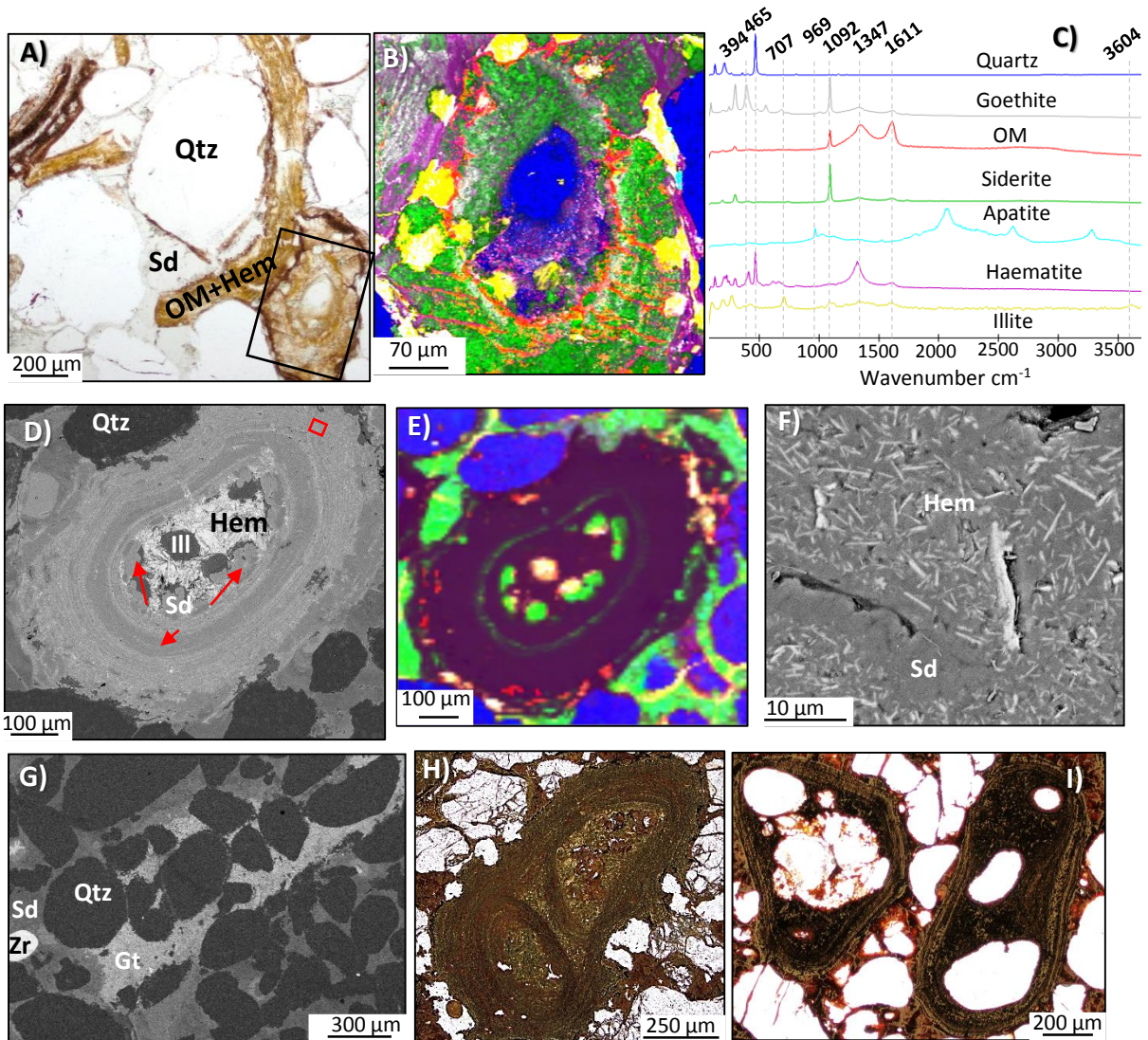


Figure 4. Concentric iron-oxide and siderite granules of the chuanlingguo GIF (*CHG1502*, *CHG1510*) A) Transmitted Light (TL) image of granule and mats of OM, haematite/ goethite, clays and carbonate. B) Raman map of granule boxed in A. C) Representative Raman spectra for this figure. D) Back scattered electron (BSE) image of haematite siderite granule. E) Raman map of granule in D. Black area is a mix of microscopic haematite in siderite, box corresponds to panel F. F) BSE image of boxed area in D. G) Backscatter image of detrital quartz and zircon grains. H) Doubly bound haematite+goethite granules without a central core. I) Haematite+goethite granules formed around multiple detrital non-centred quartz grains. Qtz = Quartz, Ill = illite, Hem = Haematite, Gt = Goethite, Sd = Siderite, OM = organic matter, Zr = zircon



**Figure 5**

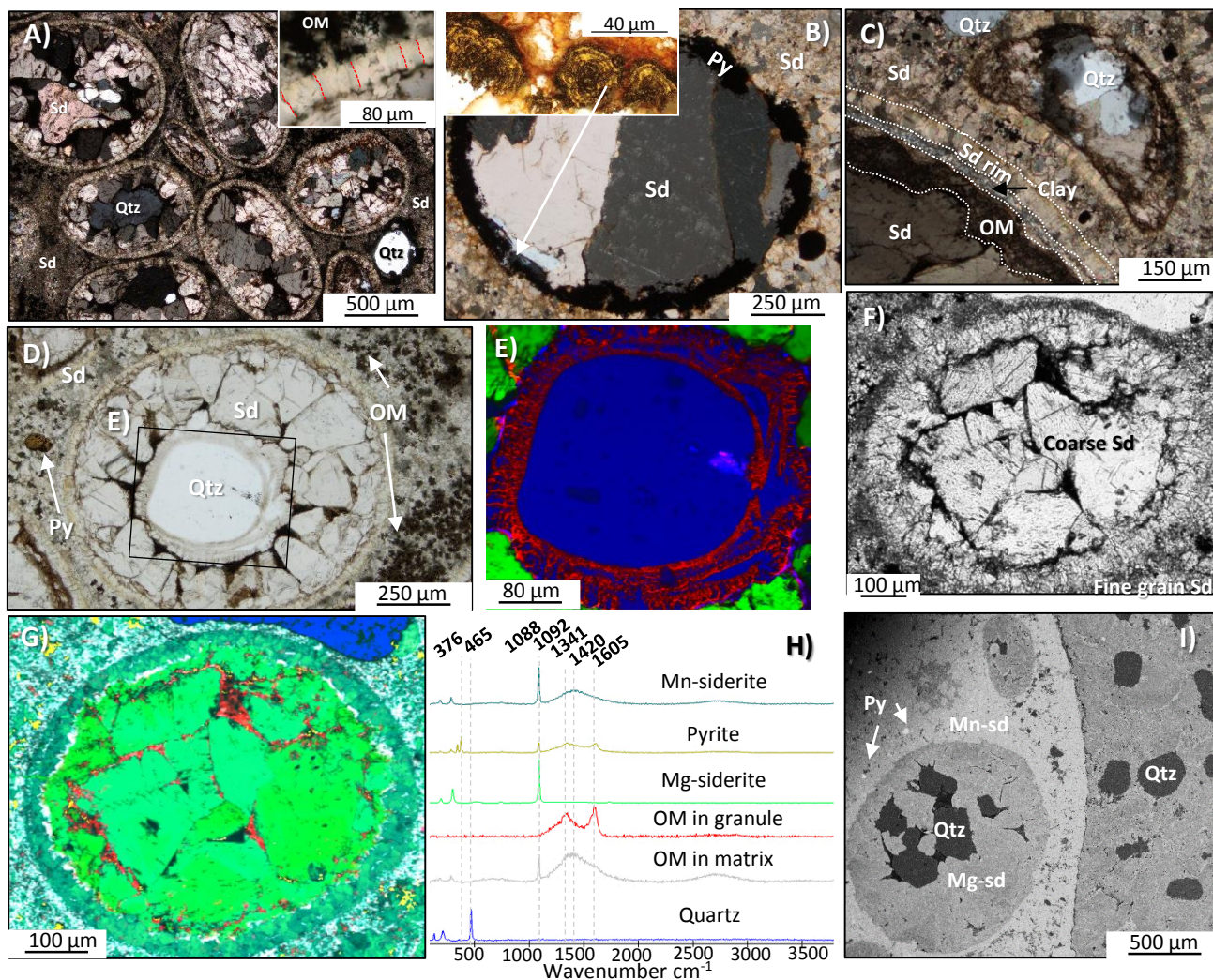


Figure 5. Pyrite-siderite granules in the chuanlingguo GIF (CHG1501). A) Siderite granules, taken in cross polars (CP). Inset shows a granule margin with outward-radiating, orientated siderite crystals delineated by red dashes. B) CP image of siderite granule that contains coarse siderite crystals relative to the matrix. The margins of the granules are formed of spherical aggregates of pyrite (inset taken in reflected and transmitted light). C) Siderite granule with layered rims of OM and clays. D) Siderite granule with detrital quartz core. OM occurs inside the granule between coarse siderite grains and in the quartz grain margin. E) Raman map of the latter detrital quartz grain surrounded by a quartz rim with outward-radiating concentric layers of OM. F) TL image of coarse siderite granule without detrital quartz. G) Raman map of siderite granule in F that shows the presence of dense OM between coarse siderite grains. H) Representative Raman spectra for the Raman images in panels E and G. I) Backscattered electron image of siderite granules that highlights the Mn-rich siderite matrix in light gray compared to Mg-rich siderite granule interior in darker gray, as well as detrital quartz in darkest gray. Py = Pyrite, Sd = siderite, Qtz = quartz.



**Figure 6**

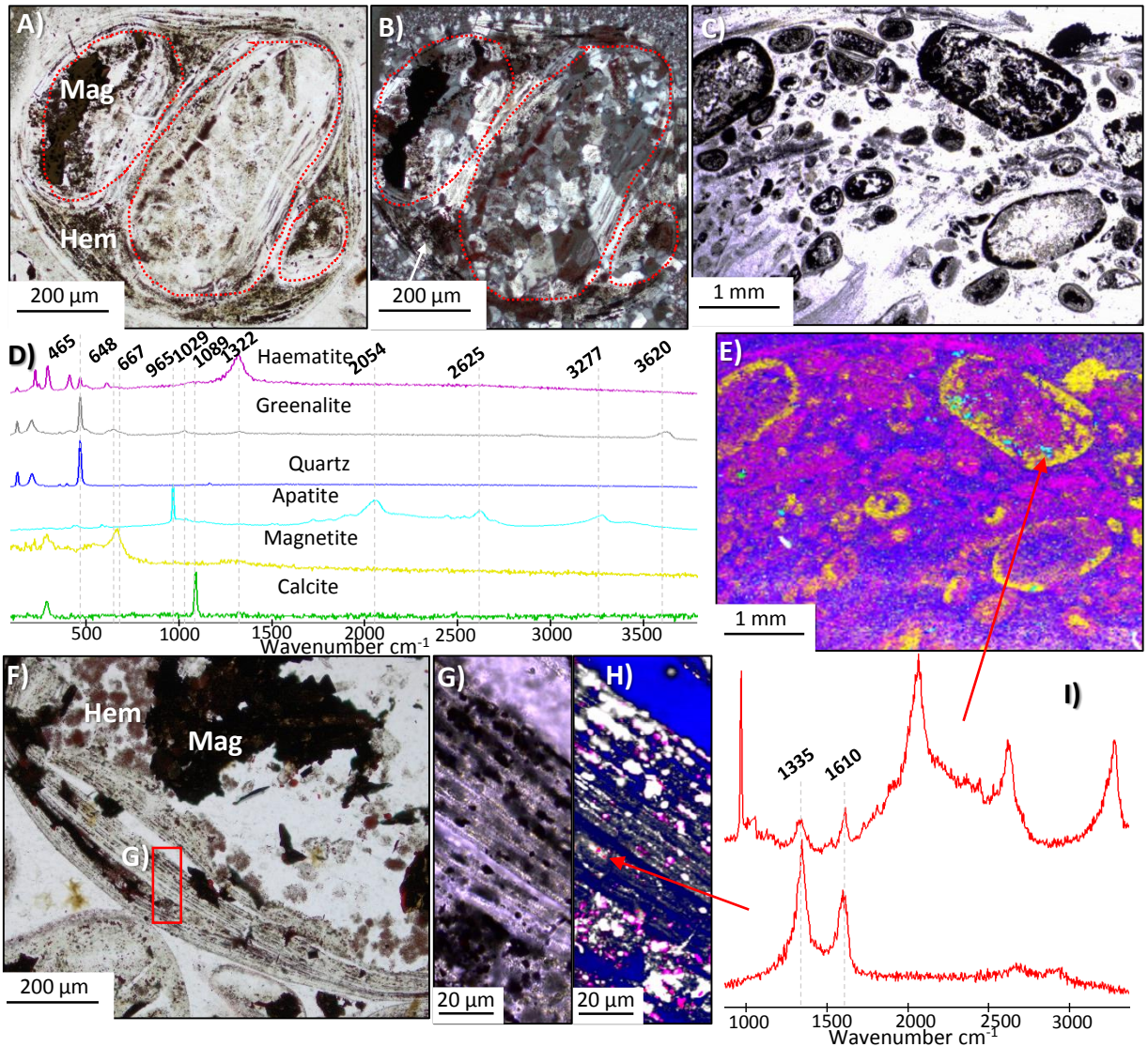


Figure 6. Magnetite and concentric rimmed granules in the Biwabik GIF from Mary Ellen mine (sample ME-B1). A) TL image of multiple bound granules. B) CP image of A showing coarser quartz within granules as opposed to the surrounding matrix. C) TL image of spheroidal granules with variable sizes. D) Representative Raman spectra for this figure. E) Raman map of C, showing the distribution of magnetite along granule rims and apatite and carbonate concentrations within the granules. F) TL image of finely laminated concentric rims around a granule. G) Increased magnification image of the concentric rims in F that shows micron-size to nanoscopic grains. H) Raman map of area shown in G with white-colour phase representing greenalite and red colour showing the location of micron-size to nanoscopic particles of OM. I) Two Raman spectra of OM inside apatite shown in E and inside quartz shown in H. Abbreviations are same as before along with Mag = Magnetite.

**Figure 7**

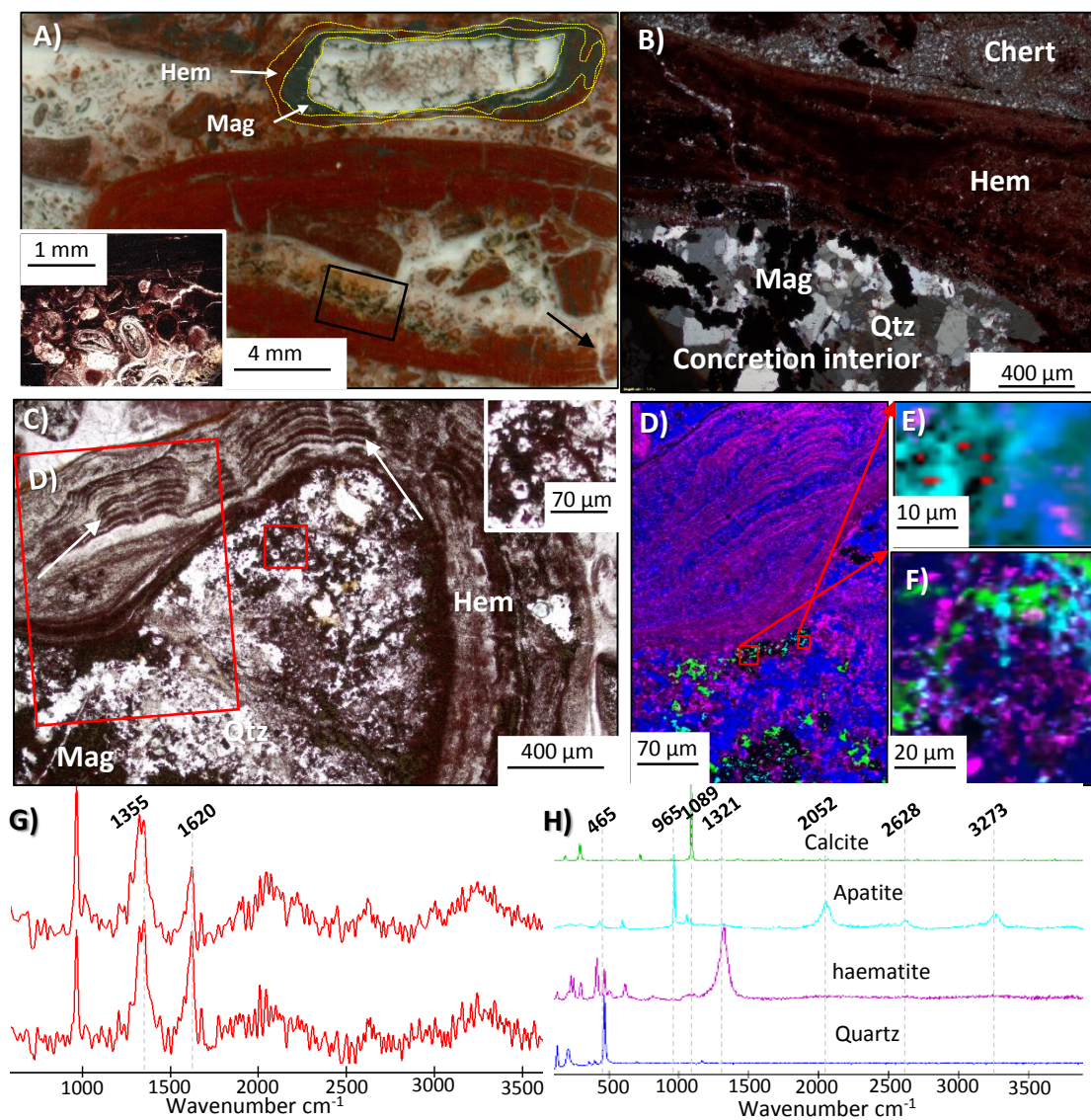


Figure 7. Stromatolitic granules and concretions from the Biwabik GIF from the Thunderbird mine (sample AG1008). A) Thin section scan of concretions with haematite and magnetite layered margins. Inset shows granules within a concretion. B) CP image a of concretion with internally coarser quartz compared to the external chert matrix. Magnetite is found within the concretion and haematite composes the rim. C) Granule with haematite, stromatolitic layering with internal haematite rosettes shown in the inset image. D) Raman image of a portion of the stromatolitic granule. E) Raman image of apatite grains inside the stromatolitic granule, which shows micron-sized inclusions of OM. F) Raman map showing the association of apatite and carbonate within the stromatolitic granule. G) Raman spectra of OM in apatite. H) Representative Raman spectra for panel D.



**Figure 8**

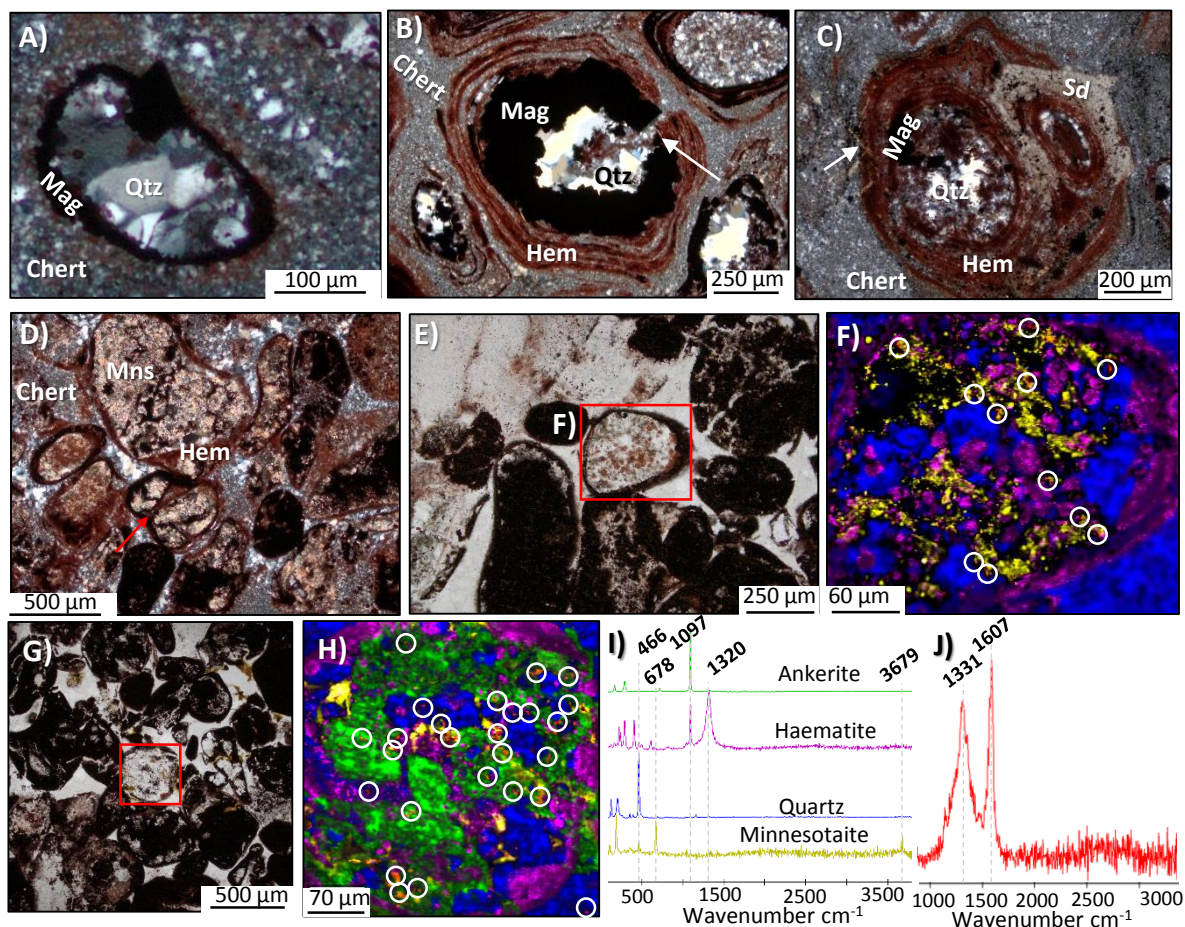


Figure 8. Magnetite rimmed granules and carbonate and minnesotaite bearing granules from the Nastapoka Gf (samples NgCi1002 and NgCi1003). A) TL image of a granule with concentric layer of magnetite and a core of coarse quartz. B) Fine concentric haematite laminations around a granule with a concentric layer of coarse magnetite and a coarse quartz centre (white arrow shows a shrinkage crack). C) Multiple granules bound by concentric laminations of haematite (white arrow points to acicular minnesotaite cutting across concentric laminations). D) CP image of granules composed of clay with rims of denser haematite. Note the binding of multiple granules by haematite rims (red arrow). E) TL image of a granule composed of clay and haematite and with microscopic spheroidal structures. F) Raman map of E that highlights the location of micron-size grains of OM (white circles). G) TL image of a carbonate granule (red box). H) Raman map of carbonate granule in G (OM in white circles). I) Representative Raman spectra for Raman maps in this figure. J) Average Raman spectrum of OM inside the granule. Mns = minnesotaite



**Figure 9**

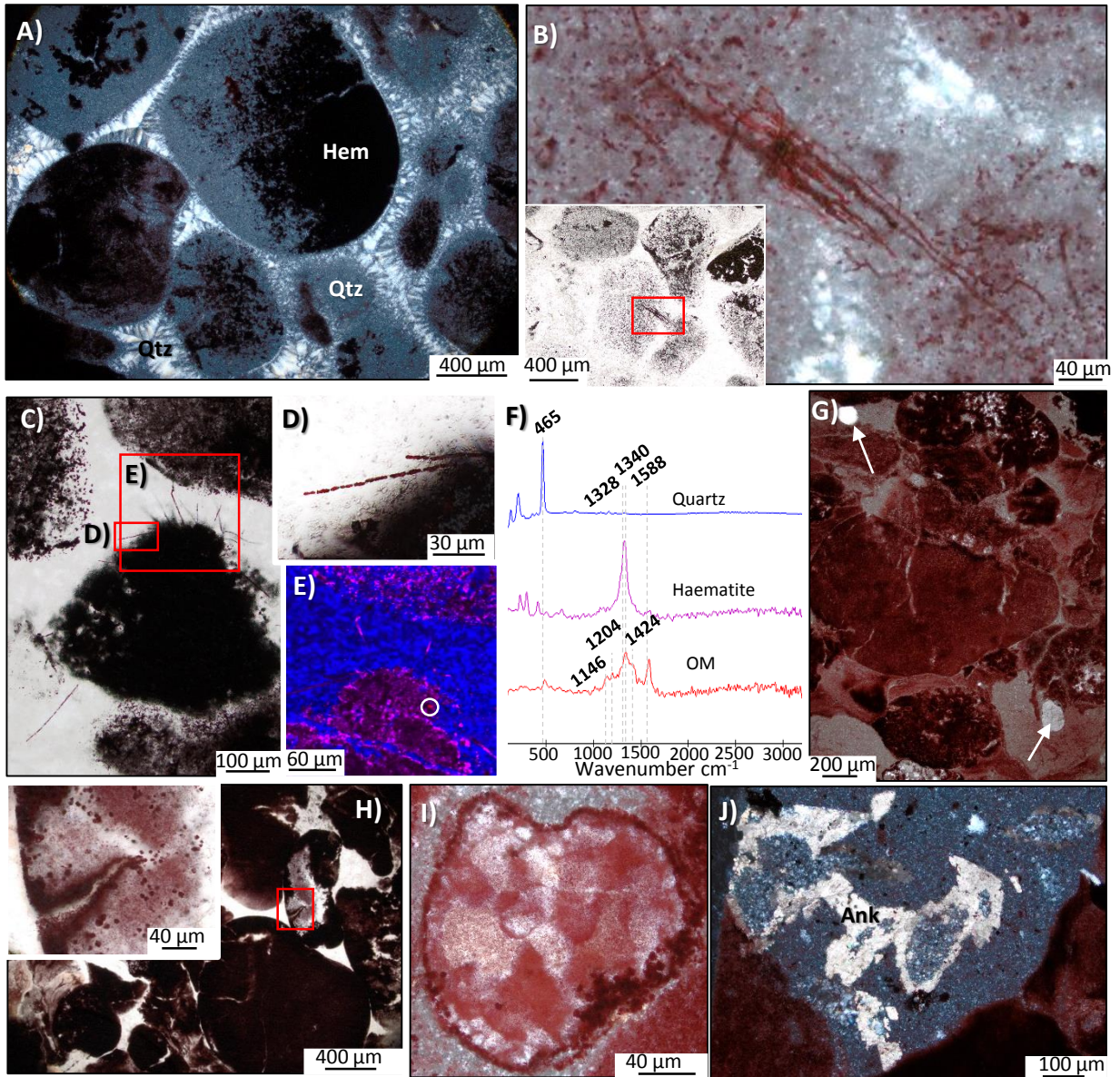
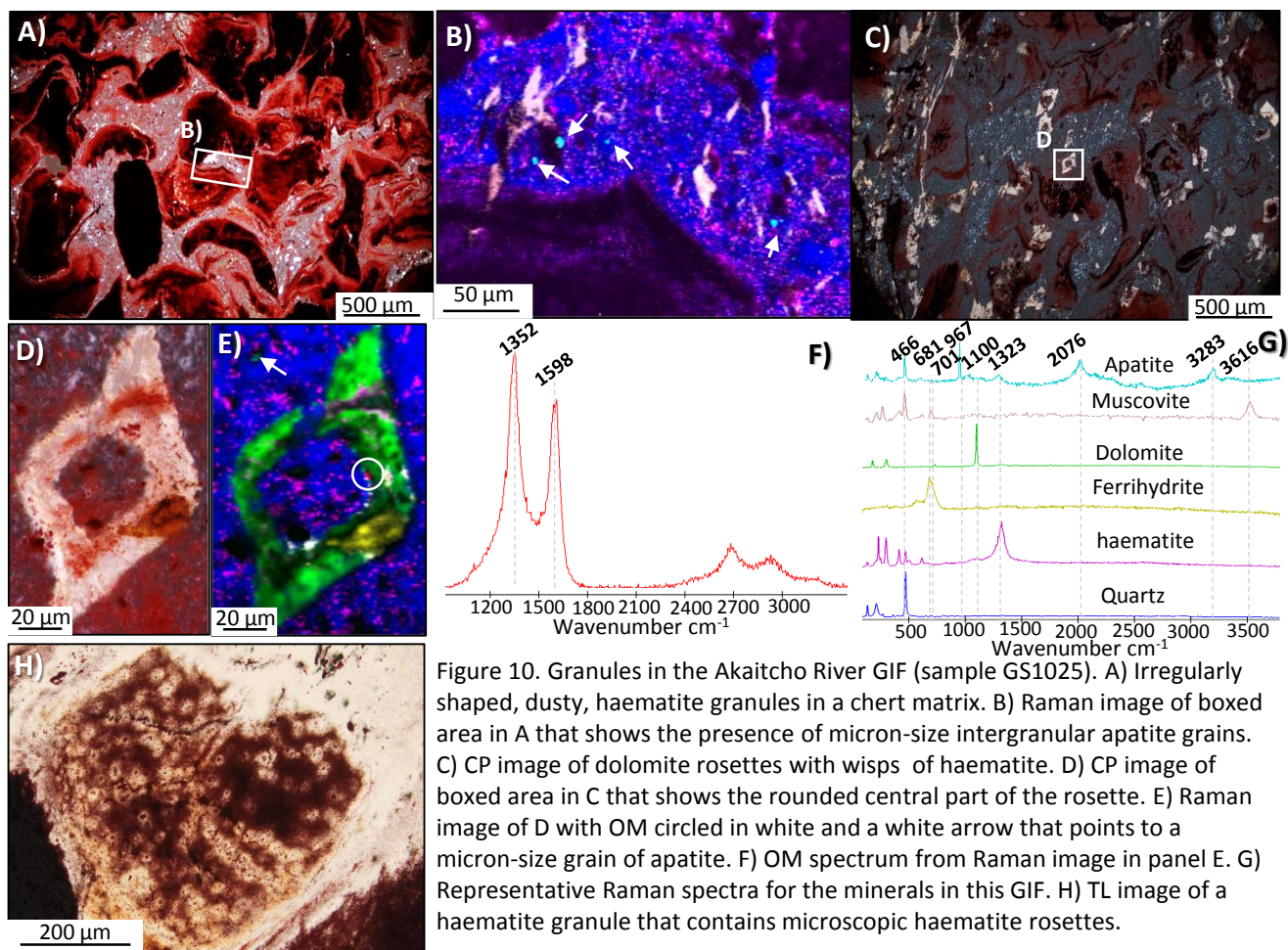


Figure 9. Granules in the Kipalu GIF (sample BgKi1002). A) Rounded haematite-chert granules in isopachous chert. Note haematite occurs mainly within granules. B) Microscopic and parallel-aligned group of haematite filaments bridging two granules. C) Haematite filaments emanating from granules. D) Increased magnification TL image of filaments in C that shows a segmented appearance. E) Raman image of granules and filaments in C, white circle highlights a micron-size particle of OM in the densest part of an haematite clump linking the group of filaments. F) Representative Raman spectra for panel E. G) Detrital quartz clasts in the chert matrix between haematite granules. H) Granule exhibiting shrinkage cracks, box corresponds to inset. I) Granule exhibiting internal quartz coarser than the surrounding matrix. J) Intergranular carbonate rosettes composed of ankerite (Ank).

Figure 10





# Figure 11

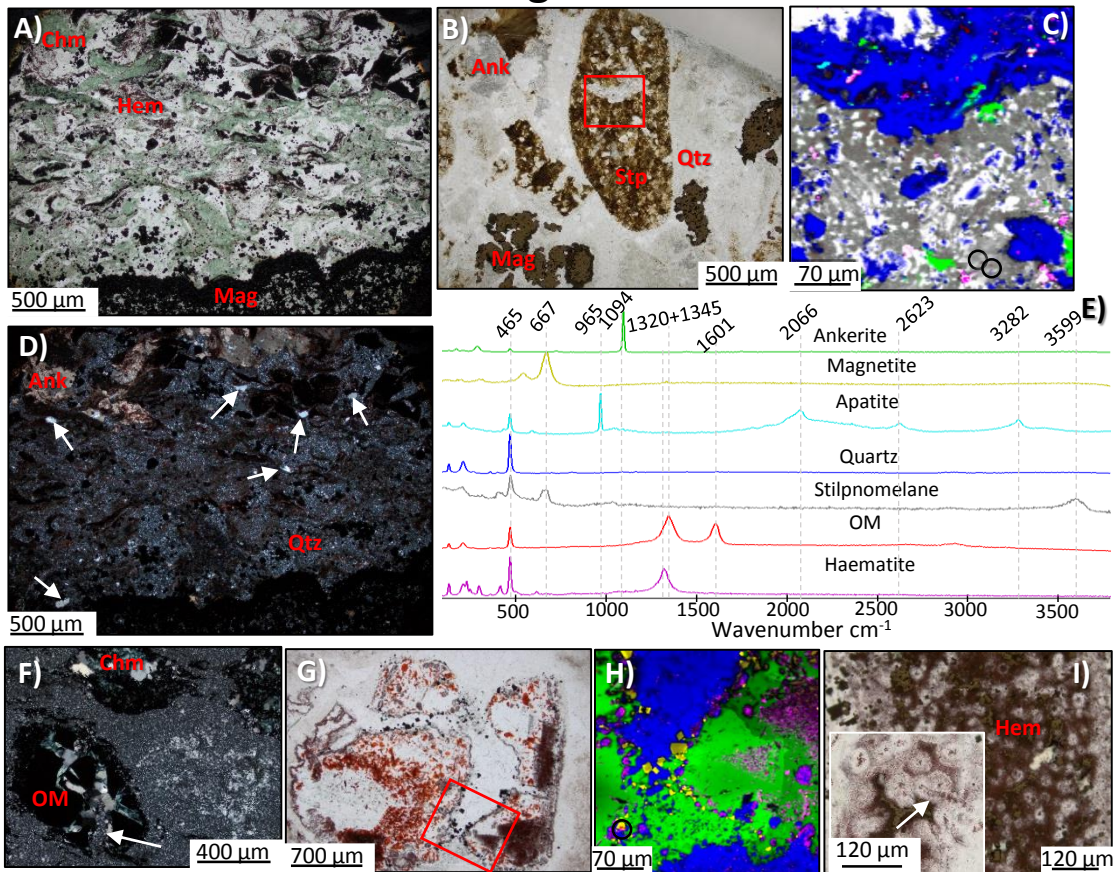


Figure 11. Granules in the Frere GIF (TDH26-series samples) A) TL image of chamosite granules with haemite rims in a chaotic mixture above a magnetite layer. B) TL image of stilpnomelane granule associated with magnetite granules and ankerite, box corresponds to panel c. C) Raman map, black circles highlight OM. D) CP image of A, arrows point to detrital quartz grains. E) Representative Raman spectra for this figure. F) CP image of OM granules with an arrow that points to a shrinkage crack. Note the coarse intragranular quartz relative to intergranular matrix. G) TL image of haematite, carbonate and magnetite granule with a box that shows magnetite inside carbonate. H) Raman image of boxed area in G that shows micron-size magnetite grains inside carbonate. I) Granule composed of haematite rosettes and, in the inset, an example of rosettes with an haematite tube shown with a white arrow . Chm = chamosite, Stp = stilpnomelane

Table 1. Elemental analyses by Energy Dispersive Spectroscopy for selected phases in selected granular iron formations.

	CHG1501	CHG1501	CHG1501	CHG1502	CHG1502	CHG1502	CHG1502	CHG1502	CHG1502	Ngci1002
	Mg-siderite	Mn-siderite	Pyrite	Siderite	Siderite	Haematite	Illite	Apatite	Zircon	Minnesotaite
C	14.7	12.9	-	11.1	11.0	-	-	-	-	-
O	34.3	30.9	5.7	38.4	31.1	18.4	38.4	37.0	36.5	49.8
P	-	-	-	-	-	-	-	21.3	-	-
F	-	-	-	-	-	-	-	4.0	-	-
S	-	-	41.3	-	-	-	-	-	-	-
Ca	-	-	-	-	-	-	-	37.7	-	-
Mg	5.5	-	-	12.7	4.8	-	1.2	-	-	15.7
Mn	-	3.2	-	-	4.3	-	-	-	-	-
Fe	45.6	53.0	53.1	37.8	48.8	76.2	6.2	-	-	7.0
K	-	-	-	-	-	-	9.4	-	-	-
Al	-	-	-	-	-	-	15.7	-	-	-
Si	-	-	-	-	-	-	29.1	-	16.7	27.5
V	-	-	-	-	-	1.6	-	-	-	-
Ti	-	-	-	-	-	3.9	-	-	-	-
Zr	-	-	-	-	-	-	-	-	46.8	-
Totals	100.0	100.0	100.0	100.0	100.0	100.0	100.0	100.0	100.0	100.0

Table 2. Stable isotope measurements of OM and carbonate in bulk rock powders of granular iron formations from the six studied late Paleoproterozoic formations.

Group and formation		Sample name	TOC wt%	$\delta^{13}\text{C}_{\text{org}}$ (PDB) (‰)	$\delta^{13}\text{C}_{\text{carb}}$ (PDB) (‰)	$\delta^{18}\text{O}_{\text{carb}}$ (SMOW) (‰)
Animikie Group, Biwabik Formation		AG1008	0.03	-28.6	-	-
		AG1008	0.02	-27.6	-	-
		Mary Ellen B	0.04	-27.8	-12.3	+18.1
Belcher Group, Kipalu Formation		Bgki11002	0.03	-28.0	-9.0	+21.4
		Bgki11002	0.02	-28.8		
		CHG1501	0.21	-27.9	-9.3	+22.3
Changcheng Group, chuanlingguo Formation		CHG1501	0.16	-29.9		
		CHG1502	0.04	-21.7	-8.5	+21.1
		CHG1507	0.02	-26.0	-	-
		CHG1510	0.03	-28.0	-7.6	+15.2
Great Slave Supergroup, Akaitcho River Formation		GS1025	0.03	-28.0	-5.1	+14.7
		GS1026	0.04	-26.7	-6.7	+19.4
Nastapoka Group, Clark Island		Ngci1002	0.02	-26.4	-	-
		Ngci1003	0.27	-36.1	-	-
		TDH26-223.15	0.02	-27.7	-11.8	+14.8
Eraaheady Group, Frere Formation		TDH26-262.4	0.03	-23.8	-16.3	+14.1
		TDH26-302.52	1.56	-34.3	-	-
		TDH26-383.6	-	-	-3.9	+14.7

\* Where values are absent, a dash mark is used to indicate values below the detection limit.

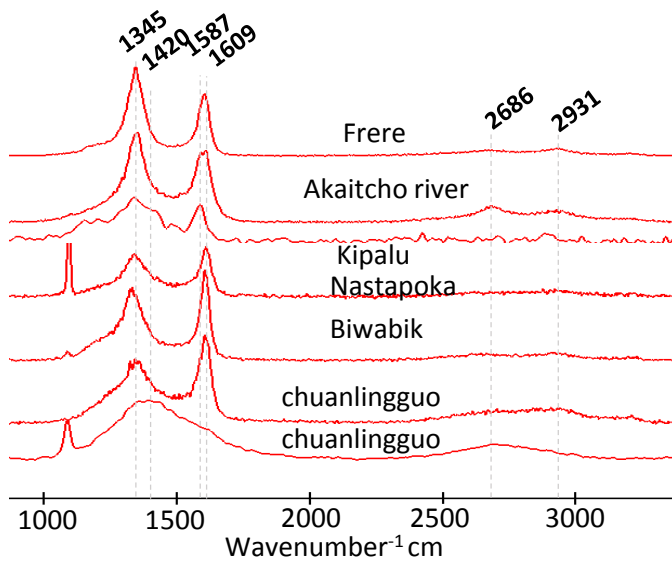


Figure 12. Summary of Raman spectra of the various types of OM identified in palaeoproterozoic GIFs

Table 3. Spectral parameters from Raman spectra of OM on Lorenz-fitted peaks along with calculated peak metamorphic crystallisation temperatures (Lahfid et al., 2010; Rahl et al., 2005)

	D1-band position	D1- band FWHM	D1-band height	G-band position	G-band FWHM	G-band height	D2-band Position	D2-band FWHM	D3-band Position	D3-band FWHM	D4-band Position	D4-band FWHM	D1-band area	G-band area	D2-band area	D3-band area	D4-band area	T Estimate Lafid	T Estimate Lafid2	T Estimate Rahl
CHG1501	1349	160	175	1607	59	250	1620	59	1510	200	1245	150	48000	22000	9000	21500	13000	202	198	274
CHG1502	1347	175	119	1605	80	151	1620	50	1510	300	1245	240	33000	17000	1000	9000	3000	245	236	250
ME-B2	1345	84	340	1596	55	230	1620	30	1510	250	1245	300	53000	22000	1000	27000	20000	272	264	291
ME-B1	1333	110	129	1604	45	162	1620	30	1510	240	1245	200	22277	11119	1000	10000	10000	272	264	251
Ngci1002	1346	146	31	1606	57	38	1620	30	1510	300	1245	250	6663	3205	200	2000	2000	300	296	239
Ngci1002	1344	160	48	1599	70	68	1620	20	1510	300	1245	300	13000	7500	200	6000	6000	257	248	254
Kipalu	1363	140	26	1597	68	24	1620	30	1510	400	1245	300	4812	2074	500	3000	2000	218	212	295
Great slave	1350	90	205	1589	43	162	1620	43	1510	100	1245	270	22300	6500	5000	4000	4000	317	317	310
TDH26 302.52	1345	78	280	1601	51	290	1620	20	1510	150	1245	300	48905	25000	3000	8000	15000	330	334	293

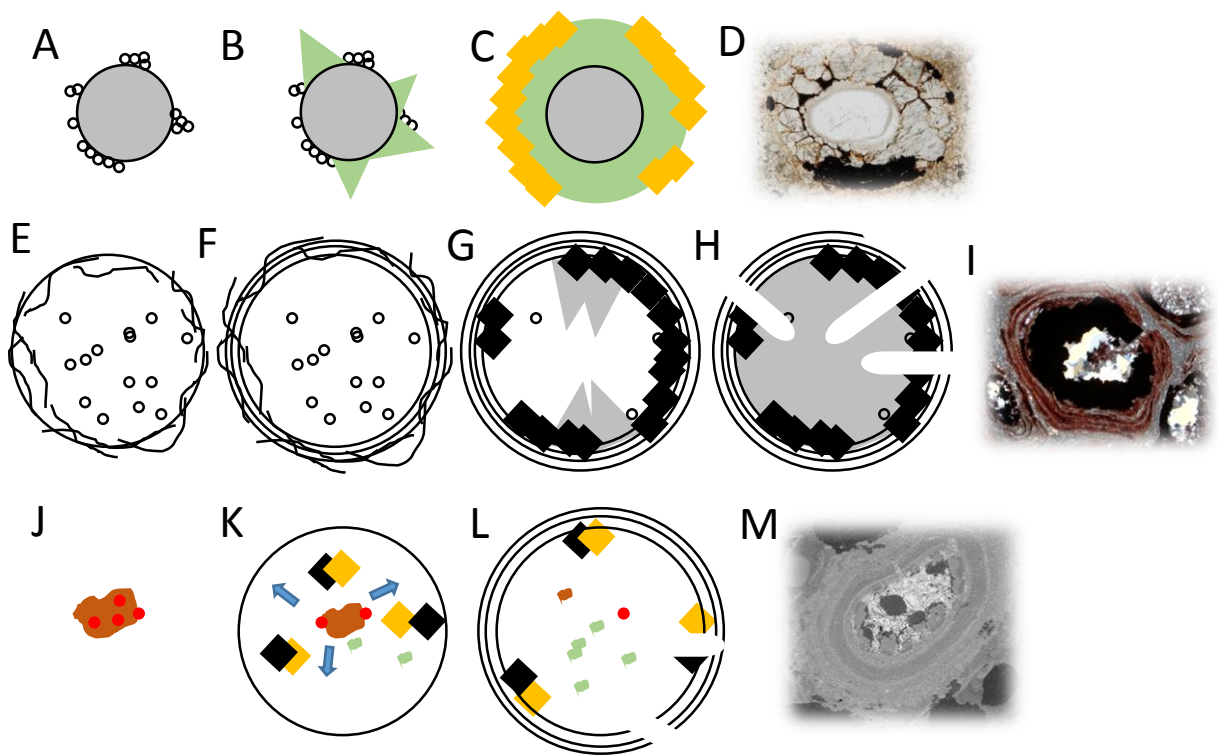


Figure 13. Models of granule formation via direct microbial activity in siderite GIF (A-D), iron-oxide GIFs (E-I) and chemically-oscillating reactions (J-L). A) Sulphate-reducing bacteria (white disks) colonise a detrital quartz grain (grey) and utilise sulphate to oxidise OM. B) Bicarbonate is produced and slowly forms siderite crystals (green). C) Diagenetic pyrite (yellow cubes) forms along rims of siderite granules. D) TL image of pyrite-siderite granule interpreted to have formed by this process. E) Colony of microbes (black circles and filaments) formed in sediments. F) Bacterial growth builds concentric layers of iron-oxyhydroxides (black circles). G) Reduction of iron-oxyhydroxides with microbial OM produces magnetite rims (black cubes) during later diagenesis either via microbial or abiotic redox reactions, production of volatiles keeps granules fluid-rich and promotes slow growth of large quartz grains (grey). H) Dehydration of the granules produces septarian cracks (white lines) cutting through the layers and the coarse quartz interior. I) TL image of iron-oxide granule interpreted to have formed by such processes. J) Microbial OM and extracellular polymeric substances (brown) deposited in the sediments under oxidising conditions (red). K) Oxidation of OM with ferric iron or sulphate produces chemical waves in the sediments pushing outwards reaction products (magnetite or pyrite – black or yellow cubes) that form carbonate minerals as the reaction proceeds (green). L) Cessation of reaction leaves reaction products around the granule rims along with other phases such as ferric oxyhydroxides which preserves chemical wave patterns.

Table 4. Comparison of observations compatible or not with the three models discussed for the formation of granules.

Observations	Figure	Wave agitation model	Chemically-oscillating model	Biological model
Rounded structure	4D;5A;6C;7I;8B;9A	Yes; Consistent movement of granules along the sediment surface	Yes; A rounded structure is predicted from chemical waves during OM oxidation	Yes; Biological growth around a core could lead to growth of microbial layers
Fine laminations	4D;6A;7J;8B	No; Wave movement is unlikely to preserve fine laminations around granules	Yes; A chemical oscillatory model based on a BZ type reaction could produce fine laminations	Yes; Microbial growth often produces fine laminations in microbialites
Discontinuous rims	7A	Yes; Wave movement can produced irregular broken edges around granules	No; A chemical oscillatory model predicts regularly spaced rims	Yes; Microbial growth can produce variable layering
Reduced rims	4E;5B;6E;7B;8B;11K	No; Mechanical agitation does not lead to the formation of reduced phases along the rims of granules	Yes; Outward-propagation of reduced reaction products could form reduced phases along granule rims	Yes; Layered microbialites have anoxic interiors that could form reduced minerals along granule rims
Multiply bound granules	4H;6A;8C-D	No; Energetic movement of granules does not lead to the binding of multiple granules by fine laminations	Yes; Generations of outward-propagating chemical waves may bind multiple layered granules in additional layers	Yes; Microbialites could possibly trap and bind multiple granules
TOC/ $\delta^{13}\text{C}_{\text{org}}$	Table 2	Yes; OM could be trapped in granules from ripped up sediment	Yes; The presence of OM is necessary for chemically-oscillating reactions	Yes; The carbon isotopic composition of OM in granules is consistent with a biological origin
Carbonate rosettes / $\delta^{13}\text{C}_{\text{carb}}$	Table 2	No; mechanical agitation is not expected for form concentrically-rounded carbonate structures nor $^{13}\text{C}$ -depleted carbonate	Yes; Chemically-oscillating reactions can produce rosette structures with $^{13}\text{C}$ -depleted carbonate	Yes; $^{13}\text{C}$ -depleted carbonate can form through biological or abiological oxidation of biomass
Authigenic apatite	4B;6E;7D;11H	No; Apatite is unlikely to be concentrated within granules by wave action	Yes; Apatite may form from the oxidation of biomass during chemically-oscillating reactions	Yes; Apatite is commonly associated with microbialites
Microfossils	7J-K;9B-D	No; Wave agitation is unlikely to concentrate microfossils inside granules nor help to preserve them	Yes; Microfossils inside granules provide OM to fuel chemically-oscillating reactions	Yes; Microfossils inside granules is direct evidence for microbial activity
Septarian cracks	7I;8B;9H;11J	Yes; Septarian cracks propagate in fluid-rich granules formed by wave agitation	Yes; Chemically-oscillating reactions occur in the fluid phase and could be promoted by dehydration causing higher concentrations of reactants	Yes; Microbial respiration can concentrate fluids within granules as OM is oxidised
Internal crystal size	5A;6B;7B;8B;9I;11J,11M	Yes; Coarser crystal sizes within granules may have formed prior to lithification and rounded by wave agitation	Yes; Coarser crystal sizes within granules may be promoted as a result of fluids retained in granules by chemical gradients	Yes; Coarser crystal sizes within granules may be prompted by wet microbial micro-environments
Irregularly shaped granule	4I; 8D;10A;11A-B,11K	Yes; Irregular and angular poorly rounded granules can form from energetic traction currents along the sediment surface	No; Chemically-oscillating reactions should promote regularly-shaped granule morphologies	Yes; Irregular microbial growth may form sharp edged and irregularly shaped granules

Detrital quartz	4A;5I;9G;11D	Yes; Detrital quartz is likely to be found in wave agitated environments	Yes; chemically-oscillating reactions could form curved equidistant laminations around detrital grains	Yes; Microbial growth can occur on the surface of detrital quartz grains
Form lenses in outcrop	1G,1I	Yes; Lenses in outcrop may form as a result of current deposition of granules in deeper basins than which they formed	Yes; In-situ growth of lenses may have occurred during chemically-oscillating reactions, similarly to concretions	No; Microbial activity is not expected to produce lenses of jasper in outcrop
Stromatolites	1A,E-F	No; The presence of stromatolites in the jaspers suggests wave action was not high, although moderate wave action could produce granules	Yes; The presence of stromatolites implies there was microbial biomass to fuel chemically-oscillating reactions	Yes; The presence of stromatolites provides direct evidence for microbial activity in association with granules
Internal clays	4B,4D;6H;8D;11A, 11C,11J	Yes; Clays inside the granules may have been ripped up by wave action and incorporated into the granules	Yes; Clays may be bound to OM deposited in sediments and therefore OM oxidation could have reduced compounds then available for incorporation in clays	Yes; Microbial activity can trap and bind clay particulates in extra-cellular polymeric substances
Isopachous rims	9A	Yes; Isopachous rims demonstrate the granules were formed prior to lithification and thus possibly by wave action before deposition	Yes; Chemically-oscillating reactions during diagenesis could produce spheroidal structures in chemical oozes prior to lithification by isopachous minerals	Yes; Granules formed by microbial activity could have isopachous rims that formed during late diagenesis